University of Alberta

Adsorptive separations on titanosilicate by breakthrough analysis

by

Ji hong Kim

A thesis submitted to the Faculty of Graduate Studies and Research
in partial fulfillment of the requirements for the degree of

Master of Science
in
Chemical Engineering

Department of Chemical and Materials Engineering

© Ji hong Kim
Spring 2013
Edmonton, Alberta

Abstract

Titanosilicate has unique properties in adsorptive separations such as hydrocarbon separations and air separations. In this study, Ag-ETS-10 was investigated for argon free oxygen production. During laboratory scale breakthrough experiments high purity (99.7+%) oxygen was produced at 100 kPa and 25 °C, with a recovery rate greater than 30%. These results suggest that Ag-ETS-10 could be a strong adsorbent candidate for generating high purity O_2 in PSA.

Furthermore, the kinetics of Na-ETS-10 was investigated using breakthrough experiments. A breakthrough concentration profile of diluted (5+%) methane balance helium was obtained at 100 kPa and 25 ^{o}C and was fitted with Aspen adsorption simulator. The macro/ micropore mass transfer coefficients as the adjustable tuning parameters were estimated to be 261.76 (in 1/s) and 6121.87 (in 1/s), respectively. These results are very promising as they suggest the current particles are sufficiently "fast" to be used in an adsorption process near the fluidization limit of the particles.

Table of Contents

List of Tables

List of Figures

Nomenclature

Abbreviations

BV	Ball valve
ETS-10	Engelhard Titanosilicate-10
GC	Gas chromatography
IGC	Inverse gas chromatography
MFC	Mass flow controller
PSA	Pressure Swing Adsorption
PT	Pressure Transducer
SEM	Scanning Electron Microscope
TSA	Temperature Swing Adsorption

Notation

b_i	adsorption constant
c	concentration
c_o	Initial concentration
c_{bk}	Bulk gas phase concentration
c_{msk}	Macropore gas phase concentration
D_L	Axial dispersion
D_m	Molecular diffusivity
D_c	micropore diffusivity
D_b	Internal radial bed radius
H	Height of the bed
k_f	External film coefficient
K_{mic}	micropore mass transfer coefficient
K_{mac}	macropore mass transfer coefficient
K	Henry's constant
K_p	Darcy coefficient

L	Length of the column
P	Pressure
q	loading
q_{sat}	Saturation capacity
R	Gas constant
R_p	Adsorbent particle radius
R_c	Crystalline radius
t	Time
T	Temperature
v	superficial velocity
W	Wave velocity
w_k	Micropore solid phase loading of component
w_{bk}^{*}	Bulk solid phase loading of component
w_{msk}^{*}	Macropore solid phase loading of component
z	axial co-ordinate

Greek Letters

ε_p	Intra-particle porosity
ε_i	Inter-particle porosity
ρ_b	Bulk solid density of adsorbent
ρ_c	Crystal density of adsorbent
ρ_s	Particle density of adsorbent
k_f	External film resistance coefficient

Chapter 1 Introduction

1.1 Adsorptive separations in industry

Adsorptive separation processes have been broadly used in the petroleum and petrochemical industries for many important separations and purifications. Adsorption separation processes fall into two main categories: purification (removal of trace contaminants from a process stream) and bulk separation (recovery of one component from a mixture in high concentrations). Some trends in industrial purification and bulk processes are CO_2 recovery from combustion processes, H_2 recovery from fuel gas and air separation [1]. Adsorptive separation generally follows the classification and can be categorized into Temperature Swing Adsorption (TSA) or Pressure Swing Adsorption (PSA), depending on the method of the regeneration of the adsorbent particles: (1) purging the adsorbent with hot gas in TSA, (2) reducing partial pressure in PSA.

TSA and PSA process are generally operated in a cyclic batch process; they commonly consist of at least two adsorbent beds, one on adsorption stage and the other one on regeneration stage. PSA processes are employed in much faster cycles than TSA processes as pressure can be changed much faster than temperature. Therefore, PSA enables higher throughputs than TSA the same amount of adsorbent. Simulations of the processes are generally employed to estimate the operating cost and capital

cost of the processes. It often requires understanding the dynamics of the absorbers and the properties of adsorbents. [2]

1.2 Temperature swing adsorption

TSA processes are established on the cyclic variation of temperature of an adsorbent loaded column. Figure 1 shows the schematic diagram of simple two packed beds to show TSA processes in a simple way. The adsorption takes place at low temperature on the bed 1 while the bed 2 is regenerated at high temperature. When the regeneration on the bed 2 finishes and the bed 2 cools down, the feed gas is switched to the bed 2 and pass through the bed 2 producing the product gas at low temperature. Meanwhile, the regeneration takes place at the bed 1 at high temperature. The nearly continuous production of the product gas can be achieved by using the two packed beds. In commercial process, the hot purge gas stream is employed in the regeneration stage rather than a change in temperature alone in the bed. The advantages of the TSA processes are: the use for productions of the desorbates consisting of strongly adsorbed molecules; the desorbates can be recovered at high concentration. The disadvantages of the TSA process are: long cycle times (from several hours for bulk separations to several days for purifications); and thermal aging of the adsorbents due to the repeated thermal cycling.
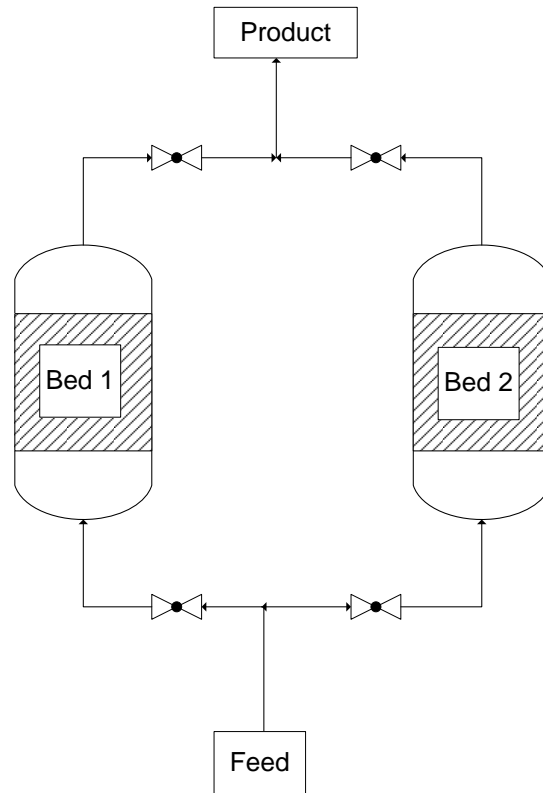
Figure 1-1. Schematic diagram of simple two packed beds

1.3 Pressure swing adsorption

PSA processes are established on the cyclic variation of pressure of an adsorbent loaded column. PSA processes can be also illustrated by Figure 1 in a simple way. The adsorption takes place at high pressure on the bed 1 while the bed 2 is regenerated at low pressure. When the regeneration on the bed 2 finishes, the feed gas is switched to the bed 2 and pass through the bed 2 producing the product gas at high pressure. Meanwhile, the regeneration takes place at the bed 1 at low pressure. The nearly continuous production of the product gas can be achieved by using the two packed beds.

In commercial process, much more complex PSA process is employed in the regeneration stage rather than simply lowering pressure alone in the bed due to the high operating cost associated with compression. The advantages of the PSA processes are the rapid cycle time and the use for productions of weakly adsorbed molecules in high purity. The disadvantages of the PSA process are: requirement for very low pressure at regeneration stage and high operating cost due to the compression; and desorbate may be recovered at low purity.

1.4 Major mechanisms of adsorptive separations

The adsorptive separation takes place through one of the three major mechanisms: equilibrium effect, steric effect or kinetic effect. The equilibrium separation is determined by the adsorbate polarizability, and sorbents with polar surfaces, dipole moment, and quadrupole moment. For instance, Kuznicki group demonstrated the equilibrium separation of CH_4 and C_2H_6 on Na-ETS-10 [3]. The pores inside the Na-ETS-10 are accessible to the CH_4 and C_2H_6 molecules because the molecular diameters of both CH_4 and C_2H_6 are smaller than the pore size of ETS-10, which has an average kinetic diameter of 8 angstrom. The pure methane raffinate streams were produced on the production stage, and the desorbed phase containing up to 75% ethane were recovered on the desorption stage.

On the other hand, the steric separation is determined by the uniform aperture size in the structure of the adsorbents and the molecular size of the diffusing molecule. The pores inside the adsorbents are only accessible to the molecules, which have smaller molecular diameters than the pore size of the adsorbent; hence the molecules can diffuse into the pores. The molecules that have bigger diameters than the pore size of the adsorbent are completely excluded and bypass the adsorbents. For instance, Kuznicki group observed the steric effect for the adsorption of ethylene and ethane on ion-exchanged forms of ETS-4 and RPZ materials. [4] The separation of ethylene and ethane on the ETS-4 and RPZ loaded column was demonstrated using gas chromatography.

The kinetic separation is determined by difference in diffusion rates of molecules inside the porous adsorbents. Slight differences in the kinetic diameters of different molecules result in relatively different diffusion rates of the molecules inside the adsorbents. For instance, PSA processes to purify oxygen using a carbon molecular sieve was demonstrated by Lee group at the Yonsei University [5]. High purity oxygen of over 99% with a high level of productivity was produced by four different PSA cycles using carbon molecular sieves loaded packed bed.

1.5 Commercial adsorbents

The adsorbents are employed in adsorptive separation processes that have been broadly used in the petroleum and petrochemical industries. The list of the commercial adsorption separation and the respective commercial adsorbents used is shown in Table 1-1 [6]. The commercial adsorbents are commonly silica gel, aluminum oxide, activated carbon, and synthetic zeolite molecular sieves. Each adsorbent has its own characteristics such as pore volume, pore structure, and the external/ internal surface area. Their usages are commonly determined by their properties. They all provide the surface areas required for selective adsorption of the favorably adsorbed species; activated carbon consists of large internal surface area of from 500 m^2/g to 1500 m^2/g; aluminum oxide contains internal surface area over 200 m^2/g; silica gel and the synthetic zeolite molecular sieve consist of large surface area about 800 m^2/g. However, activated carbon, aluminum oxide and silica gel do not possess ordered crystal structures and the uniform pores. In contrast, the synthetic zeolite molecular sieves differ from the other adsorbents in that they are crystalline and have pore openings of fixed dimensions, making them very selective. For instance, zeolite A has uniform pore size of 5 angstrom while activated carbon, aluminum oxide and silica gel have wide ranges of pore sizes from 10 angstrom to 100 angstrom.

Separation[a]	Adsorbent
Gas bulk separations	
Normal paraffins, isoparaffins, aromatics	Zeolite
N_2/O_2	Zeolite
O_2/N_2	Carbon molecular sieve
$CO, CH_4, CO_2, N_2, NH_3/H_2$	Zeolite, activated carbon
Acetone/vent streams	Activated carbon
C_2H_4/vent streams	Activated carbon
H_2O/ethanol	Zeolite
Gas purifications[c]	
H_2O/ olefin-containing cracked gas, natural gas, air, synthesis gas, etc.	Silica, alumina, zeolite
CO_2/ C_2H_4, natural gas, etc.	Zeolite
Organics/ vent streams	Activated carbon
Odors/air	Activated carbon
NO_x/N_2	Zeolite
SO_2/vent streams	Zeolite
Liquid bulk separations[b]	
Normal paraffins, isoparaffins, aromatics	Zeolite
p-Xylene/o-xylene,m-xylene	Zeolite
Detergent-rage olefins/paraffins	Zeolite
p-Diethyl benzene/isomer mixture	Zeolite
Fructose/glucose	Zeolite
Liquid purifications[c]	
H2O/organics, oxygenated organics, chlorinated organics, etc.	Silica, alumina, zeolite
Organics, oxygenated organics chlorinated organics, etc./H2O	Activated carbon
Odor, taste bodies/drinking H2O	Activated carbon
Sulfur compounds/organics	Zeolite, others
Various fermentation products/fermentor effluent	Activated carbon
Decolorizing petroleum fractions, sugar syrups, vegetable oils, etc	Activated carbon

[a]Adsorbates listed first.

[b]Adsorbate concentrations of about 10 wt.% or higher in the feed

[c]Adsorbate concentrations generally less than about 3 wt.% in the feed

Table 1-1. Representative commercial adsorption separation and the commercial adsorbents [6]

1.6 Traditional synthetic zeolite molecular sieves

Traditional zeolite molecular sieves are crystalline aluminosilicates with three-dimensional framework structures that form uniformly sized pores of molecular dimensions. The structure is formed by robust crystalline silica (SiO_2). Another building block, Al^{3+}, has substituted Si^{4+} at certain parts of the framework where carry negative charges. Zeolite structure preserves the electro neutrality as loosely held cations stay within the pore. Some of those caions are substitutable with single charged monatomic ions like Na^+ or double charged monatomic ions like Ca^{2+}, and these characteristics have led to the commercial success of the traditional zeolite molecular sieves in areas such as refining and petrochemical industries and agricultural industries.

Furthermore, zeolites are widely used in laundry detergents; synthetic zeolite with a maximum cation exchange capacity governs how well the calcium and magnesium cations in the hard wash water can be replaced with sodium cations turning the wash water soft.

Additionally, zeolites are readily used in catalytic process; synthetic zeolite with maximum acid strength governs how well the reforming, isomerization and cracking of hydrocarbon take place over the zeolites in the reactors. High Si:Al ratio is required for temperature resistances because the most of the catalytic process occurs at high temperature from 500 ^{o}C to 800 ^{o}C. Figure 1-2 shows the framework of the high-silica zeolite

ZSM-5. [7] The building blocks are connected to form pentail chains, which are linked with oxygen bridges to form corrugated sheets with 10-ring. The 3 dimensional 10-ring channel system contribute significantly to distinct selectivity sorption and catalysis compared to 8-ring or 10-ring channel system.
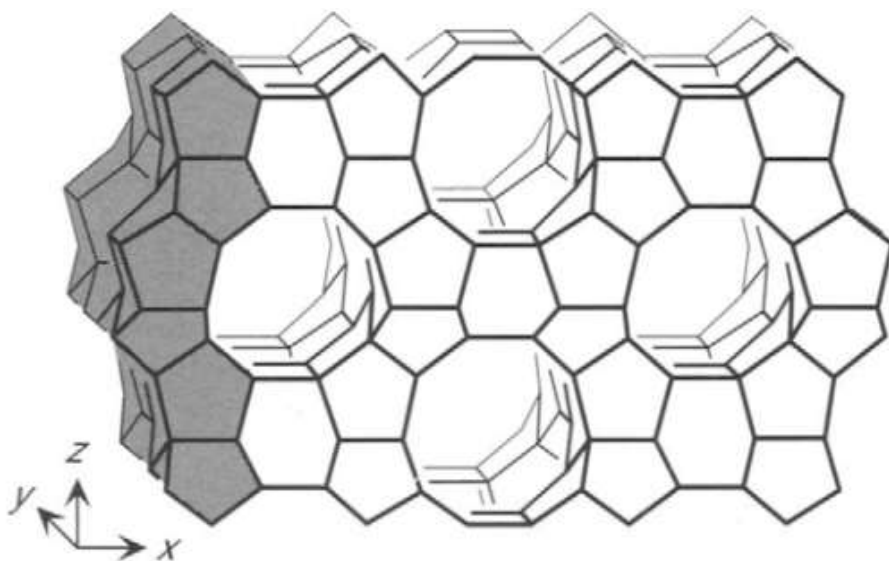
Figure 1-2. Framework of the high-silica zeolite ZSM-5 [7]

Similarly, adsorption characteristics are determined by the properties of the zeolites such as the crystalline structures, pore opening sizes, high surface areas, and adsorption capacity. The crystalline structure of the zeolite can contribute significantly to shape-selective adsorption by imposing steric hindrance on the passage of the adsorbed molecules. In addition to the traditional molecular sieves, novel synthetic structures developed, such as titanosilicates, in the hopes of generating new commercial adsorbents with new framework structure.

1.4 Engelhard Titanosilicate-10

The novel synthetic molecular sieve, Engelhard Titanosilicate-10, is a crystalline titanosilicate with a three-dimensional network of interconnecting channels. The structure is formed by mixed building blocks of octahedral (TiO_6) and tetrahedral (SiO_4). Figure 1-2 shows the structure of ETS-10. The pore structure consists of 12 membered rings and exhibits a significant degree of disorder due to different stacking sequences resulting in the broadening of the pore up to 2 nm. ETS-10 displays distinctive properties in gas separations due to its unique features of good accessibility for guest molecules and the presence of –Ti–O–Ti–O–Ti– chains electrically isolated by the siliceous matrix [8].
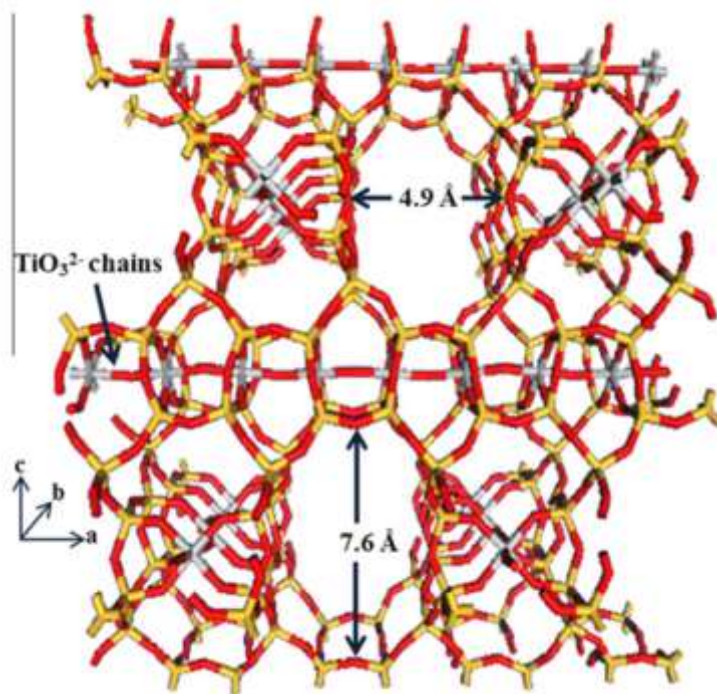
Figure 1-3. Framework connectivity of ETS-10 [8]

Each TiO_6 building block carries two negative charges, which are offset by extra framework charge-balancing cations Na^+ and K^+ in the as-made materials as specified by the ETS-10 stoichiometry $(NaK)_2TiSi_5O_{13}$ [9]. Extra framework charge-balancing cations are exchangeable, and the substitution of extra framework cations can substantially modify the adsorption characteristic of ETS-10 [10]. Kuznicki group observed that ion-exchanged form of ETS-10 such as Li-, Ba-, and Cu-ETS-10 exhibit substantial curvatures on ethylene and ethane adsorption isotherms in contrast to the Na-, K-, and Ag-ETS-10 exhibiting nearly rectangular on the isotherms.

Furthermore, incorporation of metallic silver into the ETS-10 structure gives it unique features in noble gas separation; Ag-ETS-10 has been reported as a promising potential adsorbent for the removal of argon from 95% to 5% O_2–Ar stream [11]. The adsorptive separation using a novel synthetic zeolite has been demonstrated in air separation using Ag-ETS-10 and will be discussed in detail in Chapter 3.

1.5 Experimental methods and numerical methods to measure mass transfer coefficients

A mathematical model of fixed beds is exceptionally useful for obtaining proper process designs, optimal equipment sizing, and bed. However, it is difficult to simulate the adsorptive separation process

because it requires an accurate mass transfer model of molecules in the adsorbents.

In effort to predict the separation performance, several computer simulations techniques have been developed for modeling diffusive transport in the adsorbents; Grand Monte Carlo simulation was employed to investigate the mixture adsorption in silicate [12], zeolite X [13] and zeolite A [14]; Equilibrium molecular dynamics simulation was used to study the self-diffusivity of methane in $AlPO_4$-5 [15]; Linear Driving model was employed to exam microporous diffusive transport of propylene in 5A zeolite.

In addition to the developments of numerical models, there have been numerous experimental methods established in order to support the simulation model or to measure the diffusion rate in zeolite. The conventional methods broadly vary from Zero length column by Ruthven in 1988 to NMR relaxation by Michel in 1967. The majority of these methods have been used to study the diffusion within the pores of each molecular sieve crystal while less efforts has gone into investigating diffusion within the void space between the crystals in pelletized molecular sieve adsorbents [16].

However, both the diffusion coefficients within the pores of the molecular sieve crystal and within the void space between the crystals in a pelletized adsorbent are investigated in this study. The objective of this study is to measure macro/ micro pore mass transfer coefficients in

pelletized Na-ETS-10 in the regime where the external film resistance is minimized. A mixture of 5% CH_4 balance He was introduced into a packed bed loaded with pelletized Na-ETS-10. A gas chromatography, installed with a thermal conductivity detector, was used to analyze concentration profile at the outlet. The experimental concentration breakthrough profile of methane was obtained, and the linear driving force model was used to exam macropous/ microporous diffusive transport of methane in pelletized Na-ETS-10. The Aspen adsorption simulator was employed to estimate the macro/ micro pore mass transfer coefficients by minimizing the global sum of square of errors between each experimental point and the model predicted point. Furthermore, a dead volume of the system was measured. The dead volume was incorporated into the simulation by employing different numbers of tank voids in series to correct for the diffusion effect of dead volume.

Chapter 2 Fundamentals of Adsorption

2.1 Introduction

To understand the design and operation of industrial gas separations requires at least a fundamental knowledge of the principles of adsorption and the dynamics of an adsorption column. The performance of a PSA is determined by both the equilibrium and kinetics. Most PSA processes are "equilibrium driven", implying that the selectivity depends on differences in the equilibrium affinities between each adsorbate molecule and adsorbents. In such processes, mass transfer resistance has a deleterious effect dropping the performance relative to an ideal system. The fundamental understanding of kinetics is desirable in design and operation of these processes [17].

2.2 Physical Adsorption Forces

The forces that attract the adsorbate molecules to the atoms on the surface of the adsorbent have been broadly studied. These forces are generally dispersive and electrostatic or coulombic types. The dispersive forces exist between an adsorbate and the surface of the adsorbent; the strength of the forces which depends on the nature of both the solid and the adsorbate is generally weak compared to the strength of forces associated with chemical bonding. The list of types of binding forces and the respective strength of the binding forces is shown in Table 2-1 [18].

Type of Forces	Energy (kcal/mol)
Chemical bonds:	
ionic	140-250
Covalent	15-170
Metallic	27-83
Intermolecular (van der Waals) forces:	
Hydrogen bonds	< 12
Dipole-dipole	< 5
Dipole-induced dipole	< 0.5
Dispersion	< 10

Table 2-1. Relative strengths of binding forces [18]

These weak physical adsorption forces are commonly desirable because the working capacity achievable in weak physical adsorption is high. The working capacity of the sorbent is the differential adsorptive capacity of the sorbent between the capacity at high pressure and the capacity at low pressure, or between the capacity at low temperature and the capacity at high temperature. The weak physical adsorption with the high working capacity has high process throughput rate therefore minimized the bed size and the sorbent loading resulting in low capital cost of the process. Also, the weak physical adsorption requires moderate temperature swing or pressure swing to regenerate the saturated bed thus low operating cost of the process.

2.3 Adsorption Equilibrium

Adsorption equilibrium describes the loading as function of the partial pressure exerted by the molecules adsorbed onto the surface of an adsorbent at a given temperature. For a single adsorbate, three state variables are required to fully describe the equilibrium: the temperature, the loading of the adsorbed phase and the partial pressure exerted by the adsorbed phase. The equilibrium form is presented in this study is the isotherm, the partial pressure as a function of the loading at a given constant temperature.

The majority of the isotherms can be classified into six types as shown in Figure 2-1 [19]. Type I isotherms are typical of adsorption on microporous adsorbents where only a single layer of adsorbate can form. Type II describes adsorption on macroporous adsorbents with strong interactions between adsorbents and adsorbates while Type III characterizes macroporous adsorbents with weak interactions between adsorbents and adsorbates. Types IV and V has characteristic of adsorption isotherms with hysteresis. Types VI have steps. Type I and II may be encountered in a PSA or TSA system. The resulting isotherm equations, derived from theories and models, can be used to predict the amount adsorbed based on a limited number of experiments [20].
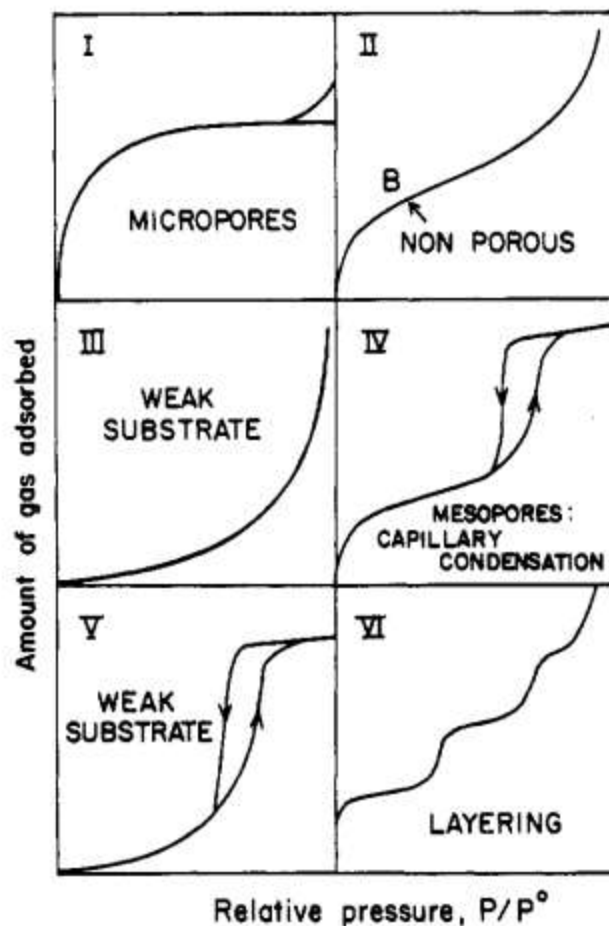
Figure 2-1. Six types of adsorption isotherm according to the 1985 IUPAC classification "Reprinted with permission from Balbuena, P. B., Gubbins, K. E., Theoretical interpretation of adsorption behavior of simple fluids in slit pores, Langmuir (1993) American Chemical Society" [19]

In this study, a microporous adsorbent ETS-10 is investigated to study the adsorption equilibrium therefore Type I isotherm is only relevant. Type I isotherms of ETS-10 have been reported in the previous studies from Kuznicki group; Type I isotherms of argon, oxygen and nitrogen at 30 °C on Ag-ETS-10 have been reported [11]; Type I isotherms of methane and

ethane at 30 ^{o}C on Na-ETS-10 have been reported [3]. In this study, adsorption equilibrium of ETS-10 will be investigated at ambient temperature and super ambient temperature.

2.4 Henry's law

The surface and the molecules interact entirely with the field gradient of the adsorbent when molecules are adsorbed in low concentrations onto the surface of a solid, and there are no lateral interactions between adjacent adsorbed molecules. The molecules that are found at the surface of the adsorbent have a higher energy than those found in the bulk. These molecules at the surface are exposed to a surface tension which decreases as a result of the formation of an adsorbed phase on the surface. This phenomenon is described in terms of the spreading pressure Π of the adsorbed phase and the difference in solid surface tensions before and after adsorption.

It is possible to describe the spreading pressure as a function of the equilibrium pressure analogous to ideal gas. The relationship reduces to the constant of proportionality between partial pressure and the amount adsorbed in the low pressure region of the adsorption isotherm, known as Henry's constant. Thus, Henry's constant is accountable for the linear variation of the amounts adsorbed with partial pressure when the concentrations of adsorbed species are low [21].

Furthermore, the Henry's Law constant, $K_i = q_i b_i$, is temperature dependent. The Henry's Law constant is expressed using the heat and the adsorbent temperature, $K = K_o \exp(-\Delta H/RT)$. This equation implies a constant heat of adsorption regardless of the loading state. This assumption is generally unusual, although it is still beneficial for predicting an approximate loading [2].

2.5 Langmuir Isotherm

The Langmuir isotherm is the simplest isotherm that describes non-linear adsorption for both physical and chemical adsorption [20]. The Langmuir equation describes the monolayer adsorption. Several assumptions are made:

- The surface containing the adsorbing site is uniform such that all of the superficial atoms of the solid can interact independently and equally.

- All adsorbing sites are equivalent.

- There are no lateral interactions between neighbouring adsorbed species.

- A single monolayer is formed without formation of a multilayer at saturation capacity.

The Langmuir isotherm for loading as a function of pressure is described by the Langmuir equation:

$$\frac{q_i}{q_{sat}} = \frac{b_i P}{1 + b_i P}$$

(1)

Where q_i is the amount adsorbed on the solid, q_{sat} is the saturation adsorption capacity, P_i represents the pressure in the gas phase, and b_i is the Langmuir adsorption constant.

The Langmuir model can be used to fit the adsorption loading for hydrocarbon that has strong affinity between the adsorbent and the molecule. Figure 2-2 shows that a Langmuir model can be employed to fit the adsorption loadings of C_2H_6 on Na-ETS-10 at temperature 298 K, 323 K and 343 K. The fitting parameters for the Langmuir model at 298 K, q_{sat} and b_i, are 1.88 mol/kg and 0.369 kPa^{-1}, respectively [3].
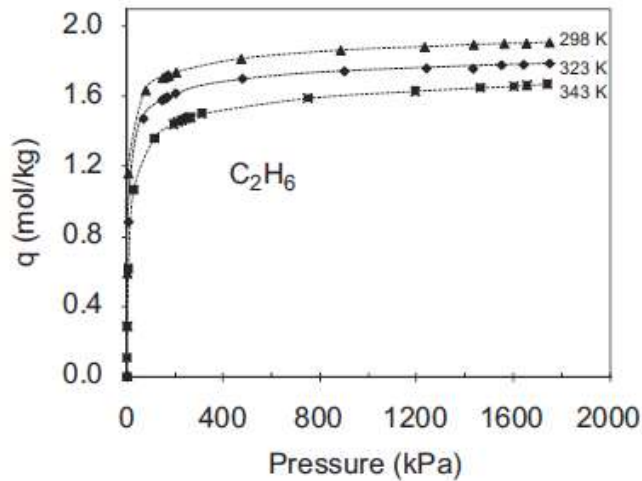
Figure 2-2. Adsorption isotherms of ethane on Na-ETS-10 at temperatures 298, 323 and 343 K [3]

The Langmuir model can be used to fit the adsorption loading for a weakly adsorbed molecule. The previous adsorption equilibrium data on Ag-ETS-10 from Kuznicki group are presented in this chapter below because the next chapter focuses on the demonstration of the air separation by breakthrough analysis. Figure 2-3 shows that a Langmuir model can be employed to fit the adsorption loadings of nitrogen, argon and oxygen on Ag-ETS-10 as a function of pressure at temperatures 30 ^{o}C [11]. The fitting parameters for the Langmuir model at 30 ^{o}C can be found in Table 2-2 [11].
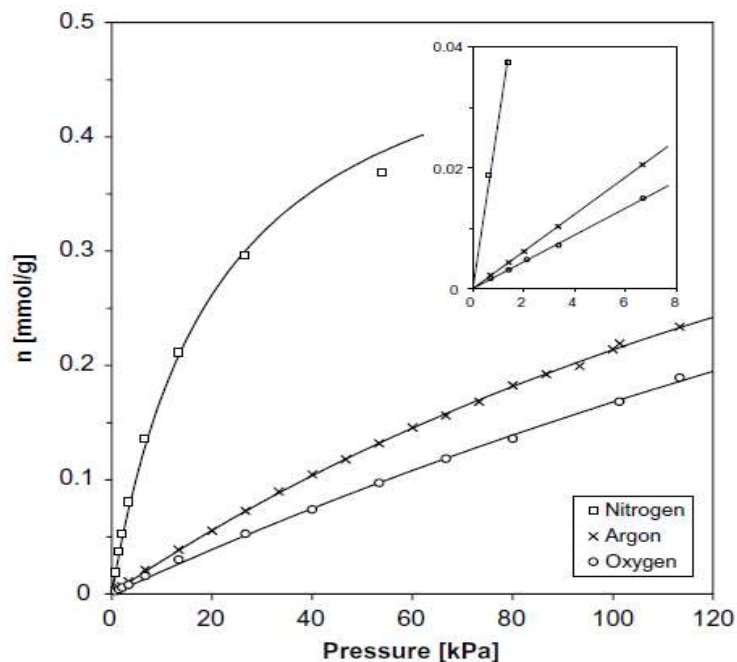
Figure 2-3. Adsorption isotherms of nitrogen, argon and oxygen on Ag-ETS-10 at temperatures 30 ^{o}C [11]

Langmuir (0–120 kPa)		Ag-ETS-10
Nitrogen	n_m (mmol g^{-1})	0.53865
	$K_L \cdot n_m$ (mmol kPa^{-1} g^{-1})	0.02546
	$\sigma \cdot 10^3$	0.108
Argon	n_m (mmol g^{-1})	0.73262
	$K_L \cdot n_m$ (mmol kPa^{-1} g^{-1})	0.00302
	$\sigma \cdot 10^3$	0.002
Oxygen	n_m (mmol g^{-1})	0.98753
	$K_L \cdot n_m$ (mmol kPa^{-1} g^{-1})	0.00202
	$\sigma \cdot 10^3$	0.004

Table 2-2. Langmuir parameters for the adsorption data in the range of 0-120k PA [11]

2.6 Selectivity

The limiting selectivity (α) of the adsorbent for gas A over gas B can be expressed as the ratio of their respective Henry's law constants in binary system, $\alpha(A/B) = K_A/K_B$.

Table 2-3 shows limiting selectivity (α) of Ag-ETS-10 and Ag-mordenite for nitrogen/argon, nitrogen/oxygen and argon/oxygen. The limiting selectivity of Ag-ETS-10 for argon over oxygen is the highest selectivity reported to date for a silver-exchanged sieve [11]. The previous adsorption equilibrium data on Ag-ETS-10 from Kuznicki group in this chapter indicates that Ag-ETS-10 is a promising adsorbent for the air separation. Thus, an adsorptive separation process has been carried out in

order to demonstrate the separation performance of Ag-ETS-10 for the air separatuib and will be discussed in detail in Chapter 3.

	Ag-ETS-10	Ag-mordenite
α (N$_2$/Ar)	8.44	4.30
α (N$_2$/O$_2$)	12.58	5.36
α (Ar/O$_2$)	1.49	1.25

Table 2-3. Limiting selectivity (α) of Ag-ETS-10 and Ag-mordernite for nitrogen/argon, nitrogen/oxygen and argon/oxygen in the low pressure range from 0 – 120 kPa [11].

Chapter 3 Air separation*

3.1 Introduction

The purification of different gases in air, such as nitrogen, oxygen and argon, is an important industrial process. Applications such as welding and cutting processes, plasma chemistry and laboratory applications require oxygen purity greater than 99%. Cryogenic air separation technology has long been used for producing high purity oxygen and nitrogen for industrial and medical applications [23] and is currently the most efficient technology when very large quantities of gas are required. The energetics and complexity of cryogenic distillation plants do not lend themselves well to point-of-use or on-demand high purity O_2 applications. PSA separation of O_2 is well suited to applications were intermittent, on-demand requirements cannot be met using bottled gas or liquid O_2 delivery. Current PSA systems cannot deliver greater than 95% O_2 due to limitations in conventional air separation adsorbents.

An air separation pressure swing adsorption (PSA) process uses zeolites as adsorbents, as they preferentially adsorb nitrogen to oxygen.[20]

24

The recovery of O_2 depends strongly on the adsorbent selected. Zeolites A and X have been used commercially as adsorbents for air separation.[24-28] A number of studies have investigated utilization of various zeolites such as Zeolite 5A and Zeolite 13X as adsorbents in PSA processes. [26, 28] In all the cases, the oxygen product purity is limited to 95% due to the presence of argon which has almost identical adsorption equilibrium properties as oxygen.

Another option to separate Ar from O_2 is by non-equilibrium methods. Another type of adsorbent, carbon molecular sieves (CMS), with a kinetic selectivity of oxygen over argon has been investigated and employed for production of purified oxygen and argon.[29-32] Ba-RPZ-3, a titanosilicate molecular sieve, was found to favor oxygen based on the sieving properties of the adsorbent and the difference in size between O_2 molecules and Ar atoms.[33] A two-step experimental study was reported by Hayashi et al. where direct air feed using Ca-X zeolite was used in the first step, producing 95% of oxygen and 5% of argon, and CMS is used in the second step to remove argon.[34] In both these studies, the O_2 is generated as the low pressure product and will require re-compression adding cost and complexity to the process.

Silver exchanged zeolites such as silver mordenite,[35] silver exchanged zeolite A,[36] silver exchanged zeolite X,[37] and silver exchanged Li-Na-LSX zeolite[38] have all been reported to show some degree of argon over

oxygen selectivity. In 2003, Air Products and Chemicals Inc. reported that a vacuum and pressure swing adsorption unit using AgLiLSX adsorbent allows the production of 99% oxygen with a recovery of 15%. [39]

In 2008, Kuznicki′s group demonstrated that silver exchanged ETS-10, a mixed coordination titanosilicate molecular sieve, has an adsorptive selectivity for argon over oxygen.[40] The selectivity , reached 1.49 in Henry′s region, is the highest selectivity reported to date for a silver-exchanged sieve.

This paper describes the adsorptive separation performance of Ag-ETS-10 for air at ambient condition on Ag-ETS-10 using a laboratory-scale demonstration unit. An adapted chromatographic method was developed to improve the quantification of O_2 and Ar in the product stream. The separation factor, breakthrough and desorption profiles are reported.

3.2 Experimental

3.2.1 Material preparation

Na-ETS-10 was hydrothermally synthesized. Preparation involved thoroughly mixing 50 g of sodium silicate (28.8% SiO_2, 9.14$ Na_2O, Fisher), 3.2 of sodium hydroxide (97+% NaOH, Fisher), 3.8 g of KF (anhydrous, Fisher), 4 g of HCl (1M), and 16.3 g of $TiCl_3$ solution (Fisher), stirring the mixture in a Waring blender for 1 h, and then transferring the

reactants to a 125 cm^3 sealed, teflon-lined autoclave (PARR Instruments) and heating at 215 ^{o}C for 64 hours. The material was then thoroughly washed with de-ionized water, and dried in a 100 ^{o}C oven.

The ETS-10 adsorbent was ion exchanged by adding 5 g of ETS-10 to 10 g of silver nitrate (Fisher, USP) in 50 g of deionized water. The mixture was heated to 80 ^{o}C for 1 hour. The silver exchanged material was filtered, washed with deionized water and the exchanged procedure was repeated two more times (for a total of three exchanges). The silver exchanged ETS-10 was dried at 80 ^{o}C in air.

The Ag-ETS-10 materials were pelletized by mixing 6 g of the molecular sieve with 2.5 g of Ludox HS-40 colloidal silica (Aldrich). The mixture was homogenized using a mortar and pestle and compressed in a pellet press at 69, 000 kPa for 3 minutes. The resulting cakes were crushed and sieved to obtain particles of the sizes between 0.85-1.68 mm.

3.2.2 Inverse-phase gas chromatography

Characterization of the adsorbent was carried out via inverse-phase gas chromatography (IGC) analysis. Figure 3-1 shows schematic of IGC. Varian 3800 gas chromatograph was equipped with a thermal conductivity detector (TCD). 4 g pelletized adsorbent were packed into 10-inch copper columns with OD of 6.35 mm. The adsorbent was activated in situ at 200 °C for 10 h under a helium flow of 30 cm^3 per minute. Gases to be analyzed

(Ar, O$_2$, 50/50 mixture of O$_2$-Ar, and air) were introduced by 1 cm^3 pulse injections into the column at 30 ^{o}C.
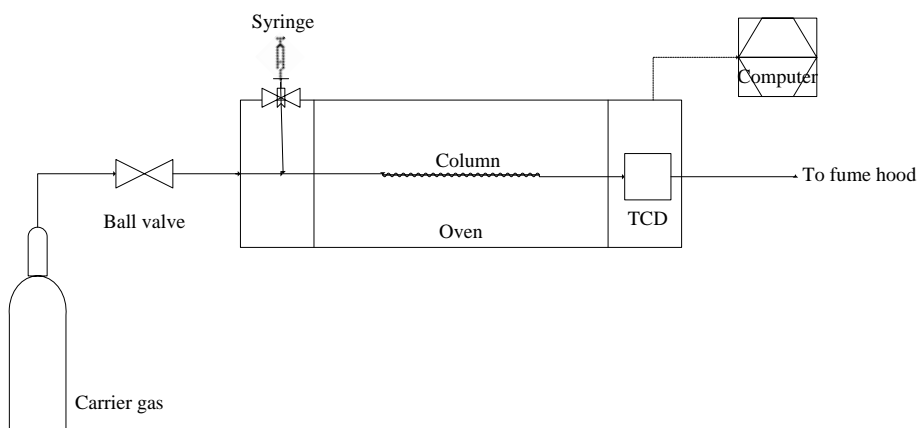
Figure 3-1. Schematic of inverse gas chromatograph

In addition to the characterization of the adsorbent, the IGC was also employed to analyse the product stream from the breakthrough experiment at cryogenic temperature. The cryogenic temperature was achieved by dipping a longer copper column in an ethanol and dry ice solution which maintained the column at a temperature close to -78 ^{o}C. The column was 50.0 cm long with an OD of 6.35 mm, and was packed with 8 g pelletized Ag-ETS-10 (sieve size between 0.368-1.04mm), which was activated beforehand at 200 °C for 10 h under a helium flow of 30 cm^3/min. The product stream from the breakthrough experiment was analysed via the IGC at the cryogenic temperature in order to identify the concentration of Ar in the production stream.

3.2.3 Breakthrough experiment

Breakthrough experiments were carried out using 130.0 g of pelletized Na-ETS-10. The adsorbent was loaded into 150 cm^3 cylindrical stainless steel column with an inner diameter of 1.9 cm and a length of 45 cm. The adsorbent was activated at 200 ^{o}C in situ for 10 hours under 100 cm^3/min of helium flow. The schematic diagram of the breakthrough experiment is illustrated in Figure 3-2.
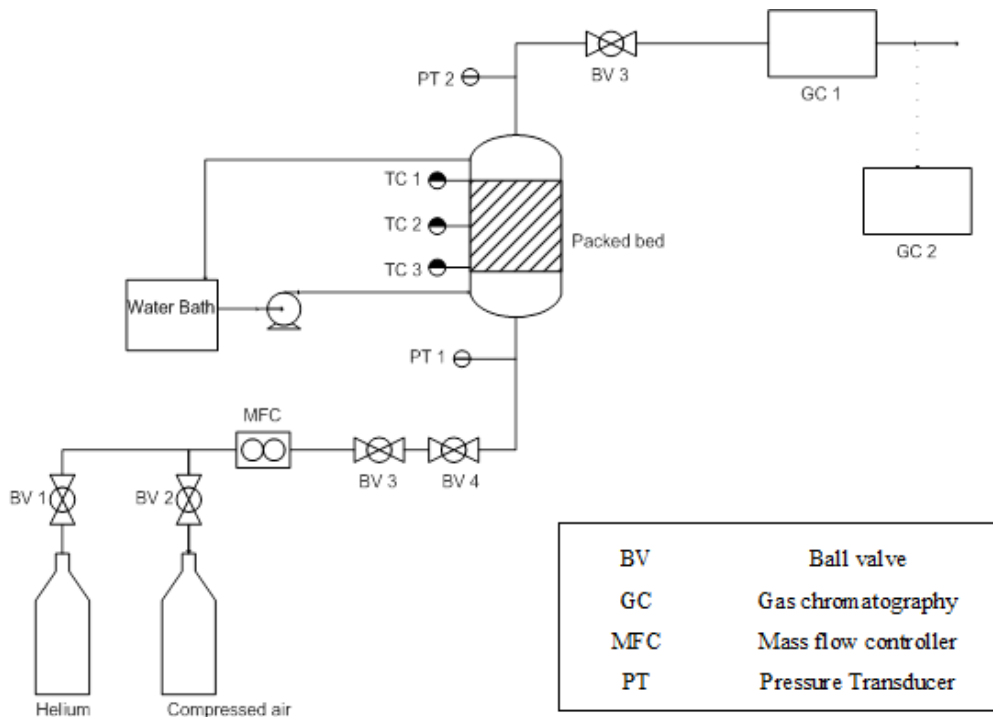
Figure 3-2. Schematic diagram of breakthrough experiment for air separation on Ag-ETS-10

The compressed air was used as the feed. The feed was introduced into the packed bed at a flow rate of 126 cm^3/min. The composition of the

air was 78% N2, 21% O_2 and 1% Ar. Parker Porter Gas Mass flow controller (MFC) was used to control the gas flow, calibrated with Coriolis mass flow meter. One ball valve (BV) was installed before each gas cylinder to switch between the feed gas and the purge gas. Before the feed gas was introduced into the packed bed, the bed was first purged with helium for about a minute to remove air in the void fraction of the bed. Two ball valves (BV) were installed before the packed bed while one BV was installed after the packed bed, controlled via customized L&C software program. One pressure transducer (PT) was mounted at the feed end of the packed bed while another PT was mounted at the outlet end of the packed bed, measuring pressure drop across the packed bed. Temperature was measured using three thermocouples installed inside the packed bed from the top layer of the adsorbent to the bottom layer. The temperature of the packed bed was maintained at 25^oC using a water jacket around the packed bed coupled to a water bath. The data acquisition was done via customized L&C software program. The outlet gas composition was analysed on two modified Varian 3800 gas chromatography (GC) installed with thermal conductivity detector. N_2 and O_2 breakthrough was analyzed via GC1 at the column oven temperature 100 ^{o}C while the Ar and O_2 breakthrough was analyzed via GC2 at the column oven temperature -78 ^{o}C.

3.3 Results and Discussion

3.3.1 IGC analysis

Figure 3-3 shows the results of IGC analysis of pure O_2 and Ar, a mixture of 50% O_2-50% Ar, and air on Ag-ETS-10 at 30 ^oC. The retention time for pure argon is approximately 2 minutes while the retention time for pure oxygen is approximately 1.5 minutes. These values indicate a preferred interaction between argon and Ag-ETS-10. This preference was also found in the analysis result for the 50% O_2-50%Ar. The analysis results of the mixtures show the presence of two peaks, with a great degree of overlap between them, indicating that the two species (O_2 and Ar) are competing for the adsorption sites in Ag-ETS-10. The analysis results for air show a retention time for N_2 at 16.5 minutes, indicating that Ag-ETS-10 has a stronger affinity for N_2 than for O_2 and Ar. The IGC results suggests that Ag-ETS-10 can effectively separate these components in air with a limiting selectivity (α) of 12.88 for N_2 over O_2, and 1.41 for Ar over O_2.
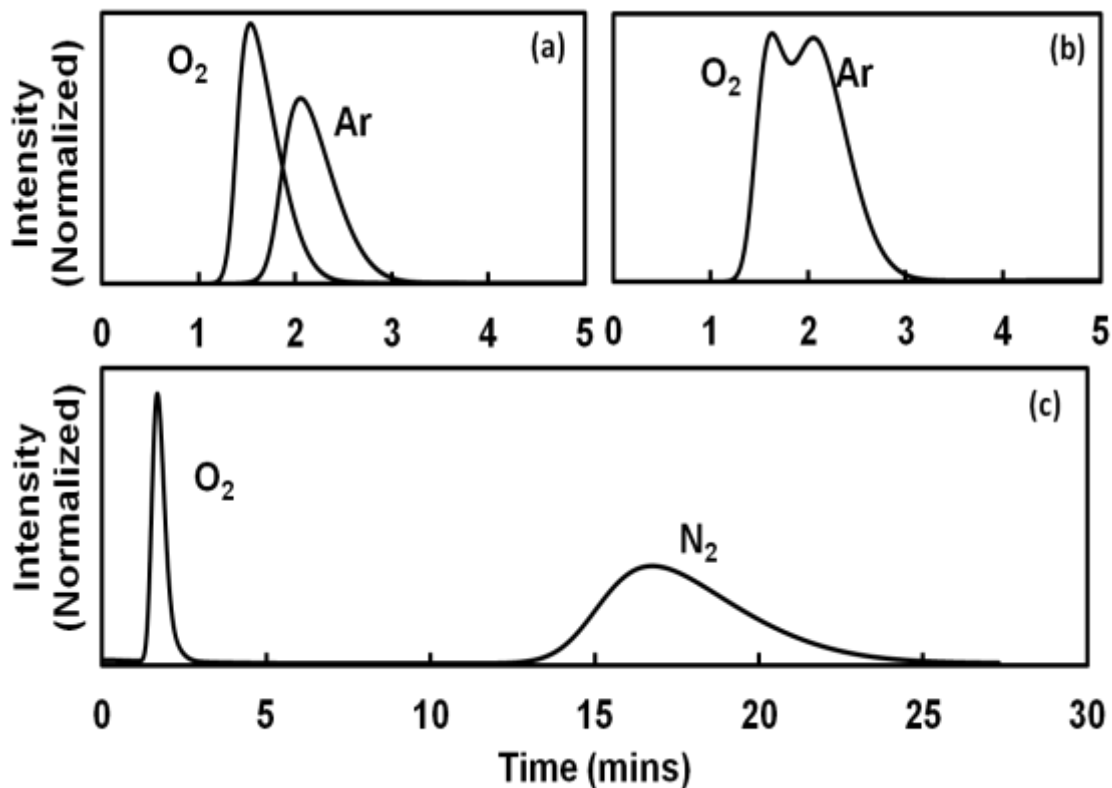
Figure 3-3. Gas chromatography separations of N_2 over O_2, Ar over O_2 on Ag-ETS-10 at 30 ^{o}C (a) pure oxygen and argon (b) 50-50% O_2-Ar mixture (c) house air

Figure 3-4 shows the results of IGC analysis of pure O_2 and Ar, a mixture of 50% O_2-50% Ar, and house air on Ag-ETS-10 at -78 ^{o}C. The retention time for pure argon is approximately 55 minutes while the retention time for pure oxygen is approximately 35 minutes. These values indicate a preferred interaction between argon and Ag-ETS-10, which is consistent with IGC analysis result at 30 ^{o}C. This preference was also found in the analysis result for the 50% O_2-50% Ar. The analysis results of the mixture show that two peaks are clearly present but with a small degree of

overlap between the O_2 and Ar peaks. This indicates that the gas kinetics at cryogenic temperature is significantly slower than the gas kinetics at 30 ^{o}C.
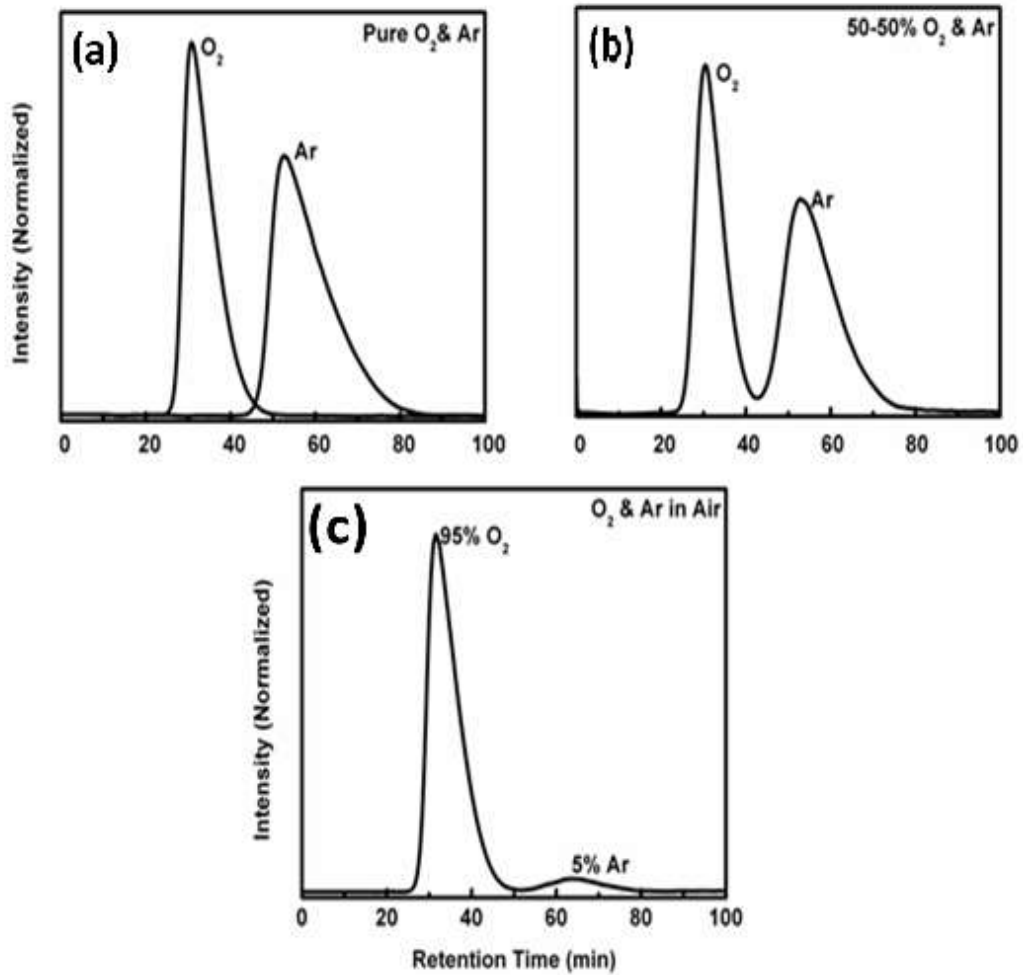
Figure 3-4. Gas chromatography separations of N_2 over O_2, Ar over O_2 on Ag-ETS-10 at -78 ^{o}C (a) pure oxygen and argon (b) 50-50% O_2-Ar mixture (c) house air

Figure 3-5 shows the IGC results for 0.3% argon and 99.7% oxygen in the product stream from the breakthrough experiment. It suggests that the Ar peak remains well resolved even at this level of purity. Thus, the

detection threshold for Ar was determined to be about 0.1%, and argon-free

oxygen in the product stream has a purity >than 99.9%.
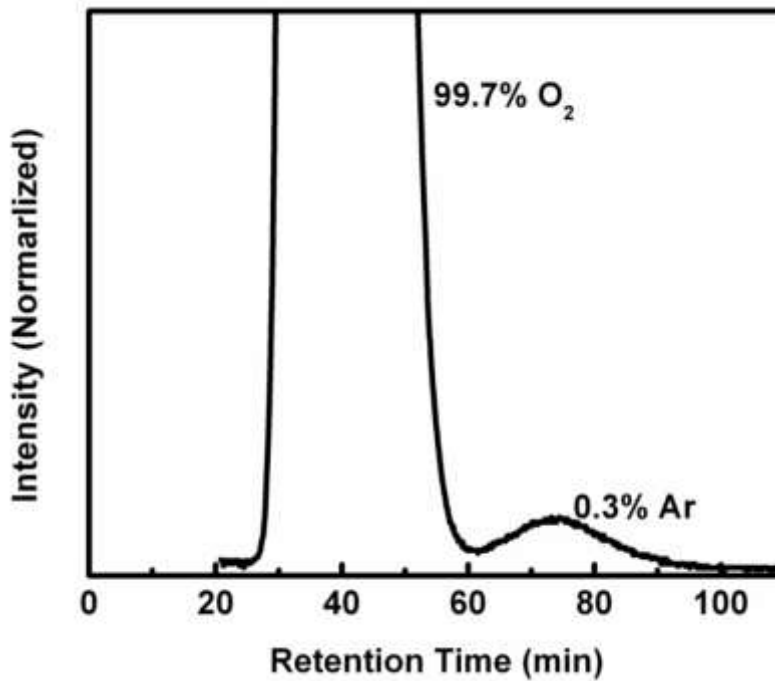
Figure 3-5. Gas chromatograph of 0.3% argon and 99.7% oxygen in the

product stream from the breakthrough experiment at -78°C

3.3.2 Breakthrough experiment analysis

The house air was introduced into the packed bed at a flow rate of

126 cm^3/min. The composition of the air was 78% N2, 21% O2 and 1% Ar.

Table 3-1 shows breakthrough concentration profiles for N_2, O_2 and

Ar on Ag-ETS-10 at 25 °C and 100 kPa. This is alo depicted in Figure 3-6:

mole fraction ratio as a function of bed volumes. The bed started producing

argon free oxygen at 11.88 min, and continued to produce an oxygen stream

with no detectable argon (<0.3% Ar) for about 1 min. At 12.96 min, 0.3 %

Ar concentration was detected, and the bed continued to produce an oxygen stream with a trace amount of Ar for about 1 min. At 15.12 min, 6.10 % Ar concentration was detected, indicating that the Ar concentration in the product stream was higher than Ar in the feed stream. This is clearly shown in Figure 3-6. One explanation for this phenomenon could be that the nitrogen molecules have displaced the adsorbed argon molecules in the bed. It suggests that the product stream contained both the desorbed argon molecules and the argon molecules in the feed stream. Thus, the detected Ar concentration in the product stream was higher than Ar in the feed stream. The nitrogen front started to breakthrough at 16.20 min. After 40 min, the packed bed was completely saturated with the house air feed.

Time (mins)	Outlet Concentration(%)		
	N_2	O_2	Ar
Feed in	78.08	20.95	0.97
0~10.80	0.00	0.00	0.00
11.88	0.00	100.00	0.00
12.96	0.00	99.70	0.30
14.04	0.00	97.00	3.00
15.12	0.00	93.90	6.10
16.20	73.75	24.10	2.15
17.28	76.08	22.70	1.22
18.36	76.52	22.31	1.17
19.44	76.84	22.00	1.16
20.52	76.98	21.98	1.04
21.60	77.05	21.92	1.03
22.68	77.10	21.87	1.03
23.76	77.13	21.84	1.03
40	77.96	21.05	0.99

Table 3-1. Outlet composition of the breakthrough for N_2, O_2, Ar at 25 ^{o}C and 100 kPa
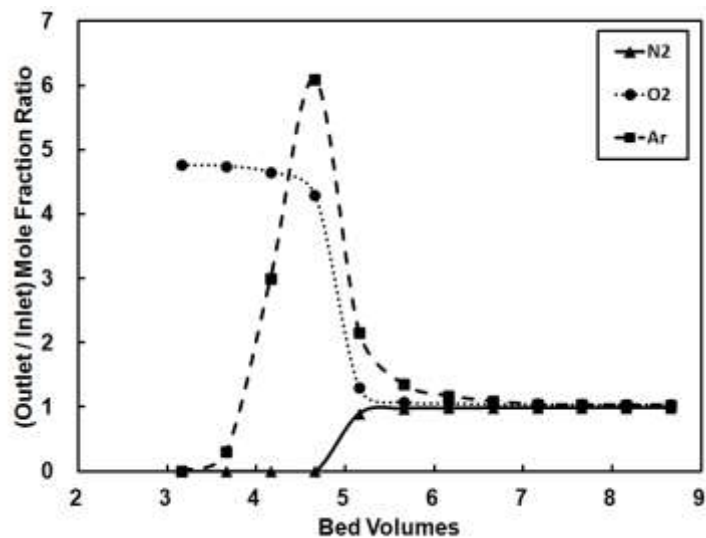
Figure 3-6. Breakthrough concentration profiles for on Ag-ETS-10 at 25 $^{\circ}$C and 100 kPa

Figure 3-7 shows the outlet flow rate monitored by Agilent ADM 1000 in adsorption procedure. The outlet flow rates for the first 10 min represented helium flow rates from the dead volume of the system. Thus, the integrated volume for the first 10 min reflects the dead volume of the system, which was calculated to be 381.5 cm^3. Breakthrough time for each molecule was determined from outlet composition of the breakthrough for each molecule. Integrating the flow measured between oxygen and argon breakthrough times it is estimated that 87.2 cm^3 of 99.7+% O$_2$ was produced.

The recovery rate of 99.7+% O$_2$ was calculated to exam the overall bed performance, and was expressed by the equation:

Recovery rate of oxygen

$$= \frac{Volume\ of\ product \times oxygen\ composition}{(Feed\ in\ flow\ rate \times Time - Dead\ Volume) \times 21\%}$$

(Given the feed flow rate of 126 cm^3/min, dead volume of 381.5 cm^3, 87.2 cm^3 of 99.7+% O_2 and 1.08 min)

The recovery rate of 99.7+% O_2 was calculated to be 33% compared to a reported 20% recovery rate of 99.9+% O_2 using AgLiLSX (Santos et al., 2007). Thus, Ag-ETS-10 is a strong adsorbent candidate for producing high purity oxygen with the high recovery rate.
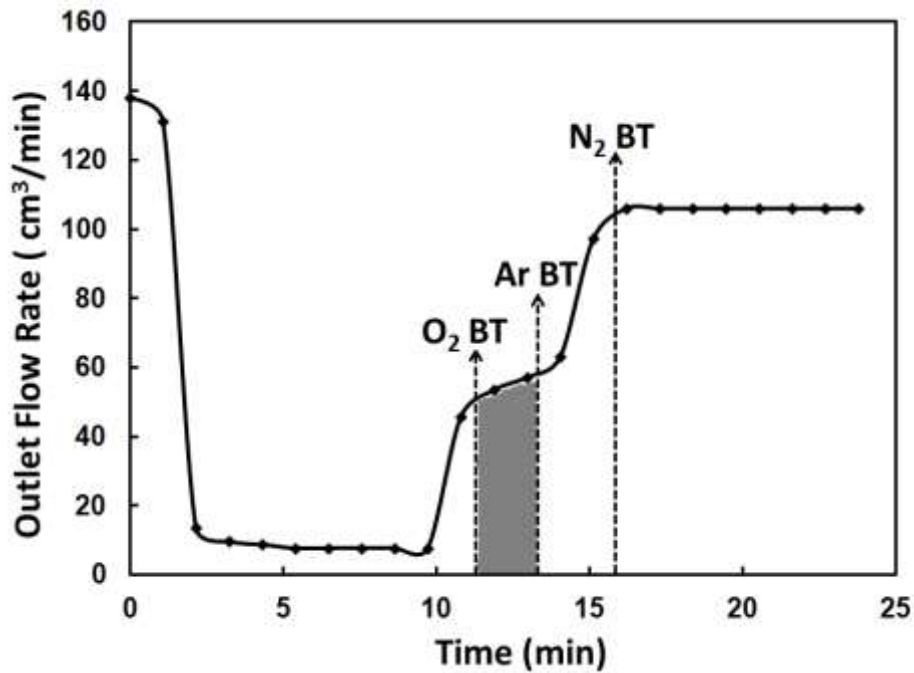
Figure 3-7. Outlet flow rate monitored by Agilent ADM 1000 in adsorption procedure

3.4 Conclusion

This study has demonstrated that Ag-ETS-10 is a selective adsorbent for argon over oxygen and nitrogen over oxygen. During laboratory scale breakthrough experiments high purity (99.7+%) oxygen was produced at 100 kPa and 25 °C, with a recovery rate greater than 30%. These results are very encouraging and suggest that Ag-ETS-10 could be a strong adsorbent candidate for generating high purity O_2 in PSA.

Chapter 4 Measurement of macro/ micro pore mass transfer coefficient of pelletized Na-ETS-10 by breakthrough simulation

4.1 Introduction

The synthetic molecular sieve, Engelhard Titanosilicate-10 (ETS-10), has been reported as a promising adsorbent in hydrocarbon separation and air separation by PSA. In order to be used in industrial PSA processes, ETS-10 has to be formed, using binders, into composite particles with binders to enhance the strength or the mechanical resistance of the particles. The composite particle consists of small crystals bound together to create a macroporous particle.

To obtain reliable PSA process designs and optimal equipment sizing, a mathematical model of fixed beds is essential. However, it is difficult to simulate the adsorptive separation process without an accurate mass transfer model of molecules in the adsorbents.

Modeling the diffusive transport of gases in adsorbents is a most challenging stage in a mathematical simulation of adsorption processes. The concentration gradients within the pores of each molecular sieve crystal and the voice space between the crystals significantly affect the diffusion rates. Pore diffusion is presumed to limit the overall mass transfer rate of the adsorber under practical conditions in industrial gas separation. The

diffusion rates in macro/ micro pores in the pelletized ETS-10 have to be precisely measured as key inputs in accurate PSA simulations.

In order to predict the separation performance several computer aided numerical simulations techniques have been developed for modeling diffusive transport in the adsorbents: Grand Monte Carlo simulation was employed to investigate the mixture adsorption in silicate [12], zeolite X [13] and zeolite A [14]; Equilibrium molecular dynamics simulation was used to study the self-diffusivity of methane in $AlPO_4$-5 [15]; Linear Driving model was employed to exam microporous diffusive transport of propylene in 5A zeolite.

Several experimental methods have been developed in the past to measure the diffusion rate in zeolites. The conventional methods vary widely vary from Zero length column by Ruthven in 1988 to NMR spectroscopy. A majority of these methods have been used to study the diffusion within the pores of each molecular sieve crystal while less emphasis has been placed on the diffusion within the voice space between the crystals in pelletized molecular sieve adsorbents [16].

The objective of this study is to measure macro/ micro pore mass transfer coefficients in pelletized Na-ETS-10 in the regime where the external film resistance is minimized. A mixture of 5% CH_4 balance He was introduced into a packed bed loaded with pelletized Na-ETS-10. The experimental concentration breakthrough profile of methane was obtained,

and was used to estimate the macro/ micro pore mass transfer coefficients using Aspen adsorption process simulation software.

4.2 Experimental

4.2.1 Material preparation

Na-ETS-10 was hydrothermally synthesized. Preparation involved thorough mixing of 50 g of sodium silicate (28.8% SiO_2, 9.14$ Na_2O, Fisher), 3.2 of sodium hydroxide (97+% NaOH, Fisher), 3.8 g of KF (anhydrous, Fisher), 4 g of HCl (1M), and 16.3 g of $TiCl_3$ solution (Fisher). Then the mixture was stirred in a Waring blender for 1 h, and the reactants was transferred to a 125 cm^3 sealed, teflon-lined autoclave (PARR Instruments) and heated at 215 ^{o}C for 64 hours. The material was then thoroughly washed with de-ionized water, and dried in 100 ^{o}C oven.

The morphological properties of Na-ETS-10 were investigated via scanning electron microscope (SEM). Figure 4-1 shows SEM photographs of Na-ETS-10 powder. It suggests that Na-ETS-10 has a cubical morphology with an average crystal radius of approximately 4 μm.
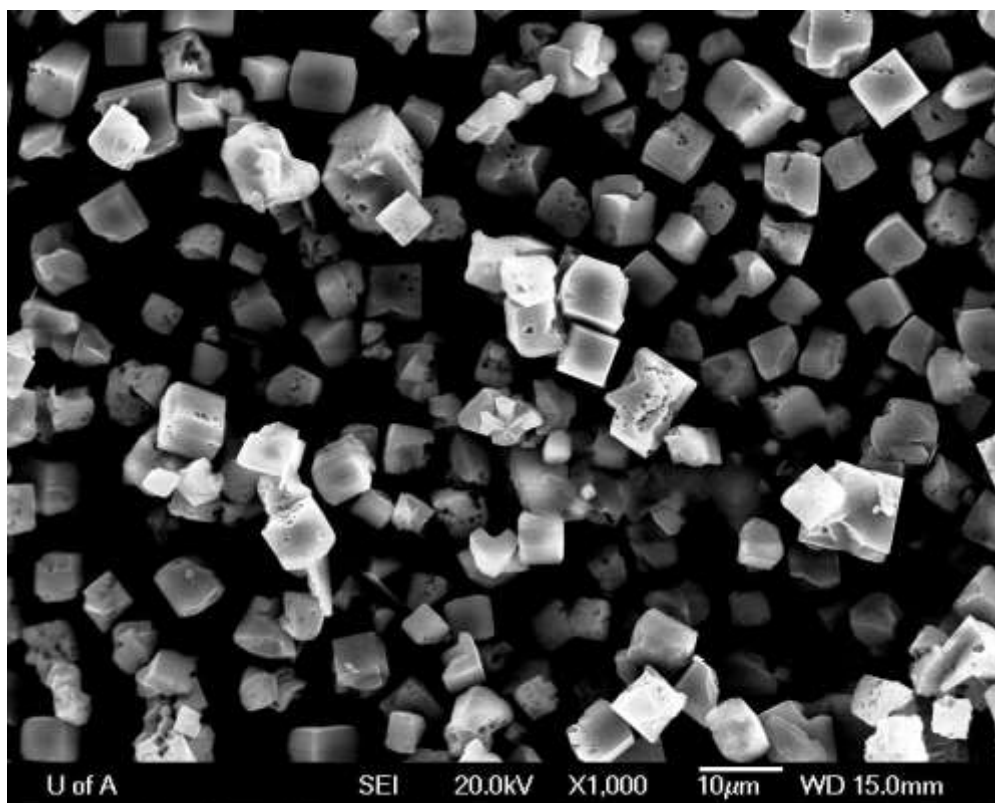
Figure 4-1. SEM photographs of Na-ETS-10 powder

The Na-ETS-10 materials were pelletized by mixing 82 g of the molecular sieve with 15 g of Ludox HS-40 colloidal silica (Aldrich) and 3 g of Acti-Gel. The mixture was homogenized using a mortar and pestle and compressed in a pellet press at 69, 000 kPa for 3 minutes. The resulting cakes were crushed and sieved to obtain particles sizes (sieve size between 0.853-0.599 mm) for breakthrough experiments on ½ inch OD packed bed.

4.2.2 Breakthrough experiments on ½ inch OD packed bed

Breakthrough experiments were carried out using 28.3 g of pelletized Na-ETS-10. The adsorbent was loaded into 40.5 cm^3 cylindrical stainless steel column with an outer diameter of 1.0 cm and a length of 45 cm. The adsorbent was activated at 200 $^{\text{o}}$C in situ for 10 hours under 100 cm^3/min of helium flow. The schematic diagram of the breakthrough experiment is illustrated in Figure 4-2, and Table 4-1 shows the physical properties of the adsorbents and the parameters for the ½ inch OD packed bed.
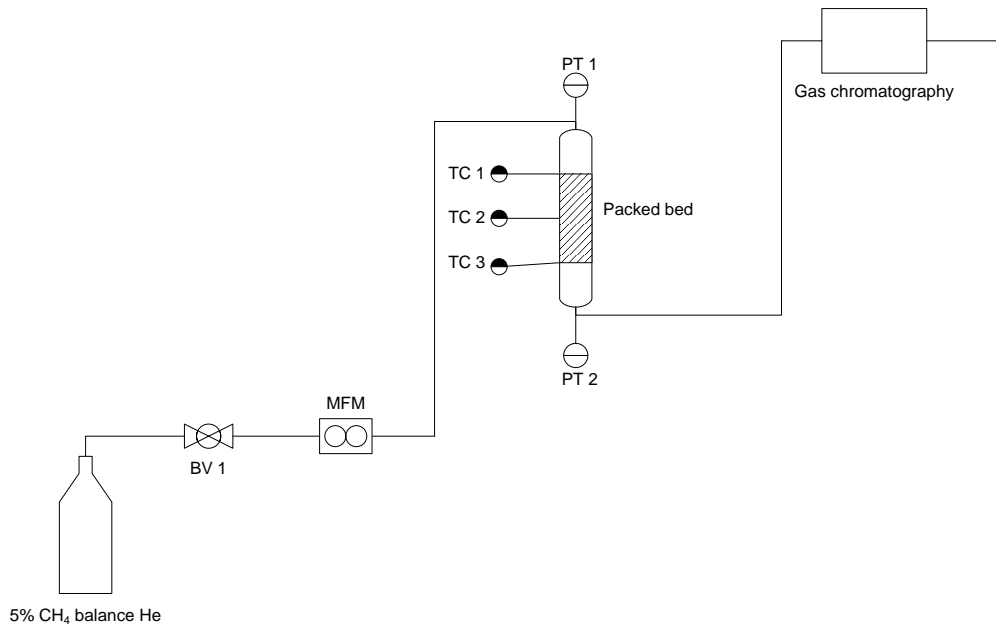
Figure 4-2. Schematic diagram of breakthrough experiment with $^1/_2$ inch OD packed bed

Variable	magnitude	Units	Description
H_b	0.5	m	Height of adsorbent layer
D_b	1.0	cm	Outer bed diameter
ε_i	0.42	m^3 void/m^3 bed	Inter-particle porosity
ε_p	0.61	m^3 void/m^3 bead	Intra-particle porosity
ρ_p	701.2	kg/m^3	Bulk solid density of adsorbent
ρ_c	2513	kg/m^3	crystal density of adsorbent
R_p	0.353	mm	Adsorbent particle radius

Table 4-1. Physical properties of the adsorbent and parameters of the $\frac{1}{2}$ inch OD packed bed

The mixture of 5% CH_4 balance He was used as the feed. The diluted methane was chosen as the analysis gas to make sure that the system was operating in the Henry's law regime. Seven different flow rates were used, ranging from 2760 cm^3/min to 14600 cm^3/min in order to minimize the external fluid film resistance. One ball valve (BV) was installed before the packed bed to control the gas flow while Coriolis mass flow meter was installed after the ball valve to measure the flow rate, controlled via customized L&C software program. One pressure transducer (PT) was mounted at the feed end of the packed bed while another PT was mounted at the outlet end of the packed bed, measuring the pressure drop across the packed bed. Temperature was measured using three thermocouples installed inside the packed bed from the top layer of the adsorbent to the bottom

layer. The data acquisition was done via customized L&C software program. The outlet gas composition was analyzed on a modified Varian 3800 gas chromatography installed with thermal conductivity detector.

The Aspen adsorption simulator was employed to estimate the macro/ micropore mass transfer coefficients numerically with the set of partial differential equations. To ensure that numerical dispersion was not limiting the system, a hundred axial discretization node was selected. The model accuracy was much improved at the cost of increasing simulation time.

4.2.3 Breakthrough experiment on 1 inch OD packed bed

Breakthrough experiments were carried out using 59.5 g of pelletized Na-ETS-10. The adsorbent was loaded into 85 cm^3 cylindrical stainless steel column with an inner diameter of 1.9 cm and a length of 30 cm. The adsorbent was activated at 200 ^{o}C in situ for 10 hours under 100 cm^3/min of helium flow. The schematic diagram of the breakthrough experiment is illustrated in Figure 4-3, and Table 4-2 shows the physical properties of the adsorbents and the parameters for the 1 inch OD packed bed.

PT 2

BV 3

Gas chromatography

TC 1

TC 2   Packed bed

TC 3

PT 1

MFC

BV 1   BV 2

5% CH$_4$ balance He
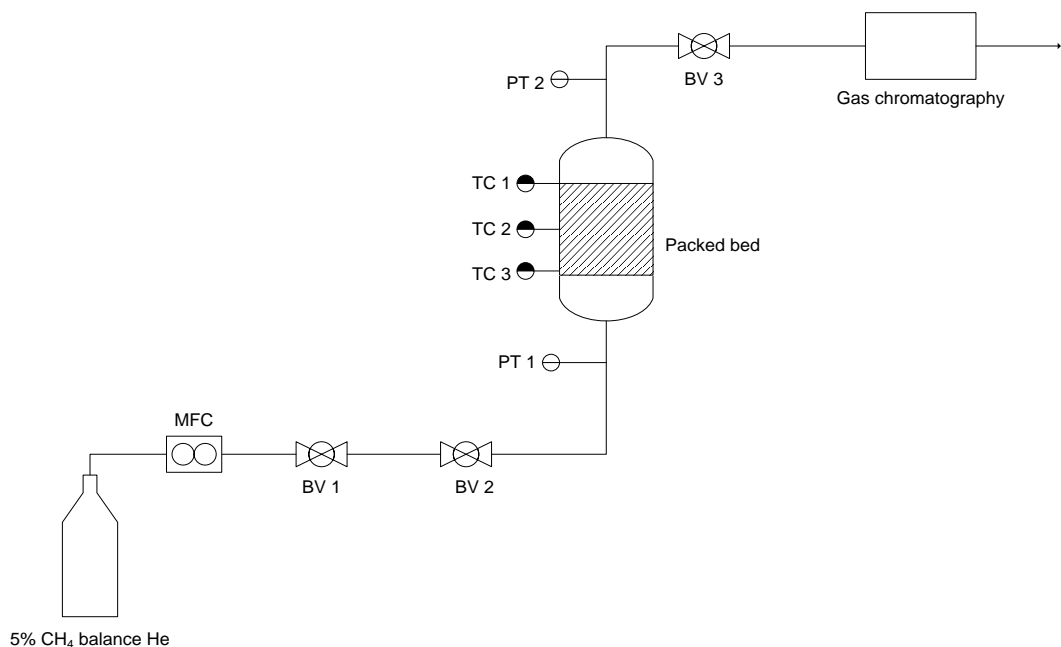
Figure 4-3. Schematic diagram of breakthrough experiment with 1 inch OD
packed bed

Variable	magnitude	Units	Description
H_b	0.3	m	Height of adsorbent layer
D_b	1.9	cm	Internal radial bed diameter
ε_i	0.61	m^3 void/m^3 bed	Inter-particle porosity
ε_p	0.42	m^3 void/m^3 bead	Intra-particle porosity
ρ_p	701.2	kg/m^3	Bulk solid density of adsorbent
ρ_c	2513	kg/m^3	crystal density of adsorbent
R_p	6.625	mm	Adsorbent particle radius
R_c	4	μm	Crystalline radius

Table 4-2. Physical properties of the adsorbent and parameters of the 1 inch
OD packed bed

The mixture of 5% CH_4 balance He was used as the feed. The diluted methane was chosen as the analysis gas to make sure that the system was operating in the Henry's law regime. Parker Porter Gas Mass flow controller (MFC) was used to control the gas flow, calibrated with a Coriolis mass flow meter. Six different flow rates were used, ranging from 6380 cm^3/min to 29800 cm^3/min. Two ball valves (BV) were installed before the packed bed while one BV was installed after the packed bed, controlled via customized L&C software program. One pressure transducer (PT) was mounted at the feed end of the packed bed while another PT was mounted at the outlet end of the packed bed, measuring the pressure drop across the packed bed. Temperature was measured using three thermocouples installed inside the packed bed from the top layer of the adsorbent to the bottom layer. The data acquisition was done via customized L&C software program. The outlet gas composition was analyzed on a modified Varian 3800 gas chromatography installed with thermal conductivity detector.

The Aspen adsorption simulator was employed to estimate the macro/ micropore mass transfer coefficients numerically with the set of partial differential equations. To ensure that numerical dispersion was not limiting the system, a hundred axial discretization node was selected. The model accuracy was much improved at the cost of increasing simulation time.

4.2.4 Adsorption Equilibrium

Figure 4-4 depicts the high pressure adsorption isotherms of methane on Na-ETS-10 at temperatures 298, 323 and 343 K (inset: low pressure adsorption isotherms at 0-10 kPA at 298 K) [3]. The adsorption data were fitted with a Langmuir isotherm model. The isotherm of methane exhibits a linear slope at low pressure (0-10 kPa), indicating that the adsorption can be expressed by the Henry's law in the low pressure ranges. In this study, 5% methane balance helium was used as the feed gas at 298 K and 1 bar in order to ensure that the adsorption equilibrium was linear.
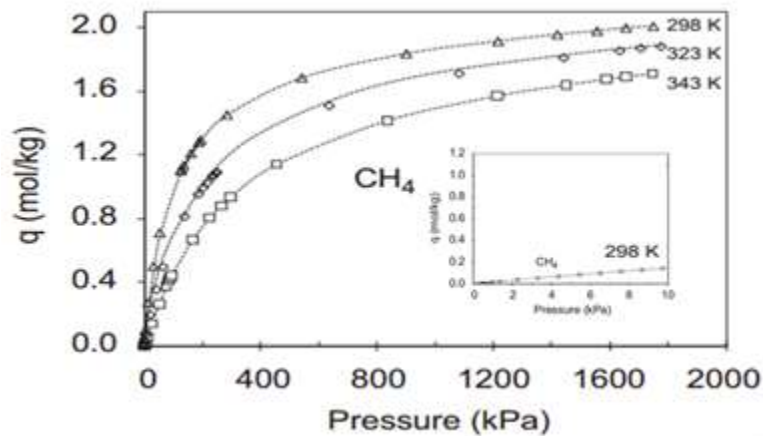
Figure 4-4. High pressure adsorption isotherms of methane on Na-ETS-10 at temperatures 298, 323 and 343 K (inset: low pressure adsorption isotherms at 0-10 kPA at 298 K) adapted from [3]

4.3 First principle analysis

4.3.1 Comparing experimental breakthrough time with predicted breakthrough time

In order to confirm that the experimental data is consistent with the adsorption data, the experimental breakthrough times were obtained from experimental breakthrough profiles when the methane concentration reaches 0.025 kmol/ kmol. Then, the experimental breakthrough time were compared with the predicted breakthrough time which was calculated by the equation (2):

$$t = \frac{L}{v}\left(\frac{1-\varepsilon_b}{\varepsilon_b} + \frac{b_i}{RT}\right) + t_{dead} \tag{2}$$

The first term and the second term on the right side of the equation are the adsorption time and the dead time, relatively.

4.3.2 Dead volume measurement

In order to measure the dead volume of the breakthrough experiment, the ½ inch OD bed breakthrough setup was used with pure hydrogen flowing at 4030 sccm. The dead time was obtained from H_2 breakthrough profiles when the hydrogen concentration reached half of the saturation concentration (0.5 kmol/ kmol). Then, the dead volume was calculated by multiplying a breakthrough time by a molar flow rates and the concentration of hydrogen, then the calculated dead volume was corrected by subtracting the volume by the volume of the bed.

4.4 Adsorption dynamics and Diffusion transport mechanisms

4.4.1 Column dynamics

The conservation of mass balance of one component for the gas phase flowing in a column is described by Equation (3)

$$\frac{\partial c}{\partial t} + \frac{\partial (vc)}{\partial x} + \frac{(1-\varepsilon_b)}{\varepsilon_b}\frac{\partial q}{\partial t} - D_L \frac{\partial^2 c}{\partial z^2} = 0 \qquad (3)$$

For high velocity the axial dispersion term was neglected and for small concentration changes across a mass transfer front, Equation (4) was simplified into:

$$\frac{\partial c}{\partial t} + v\frac{\partial (c)}{\partial x} + \frac{(1-\varepsilon)}{\varepsilon}\frac{\partial q}{\partial t} = 0 \qquad (4)$$

The uptake rate, $\frac{\partial q}{\partial t}$, is governed by both the diffusion transport mechanisms and the resistance to mass transfer.

4.4.2 Uptake in micropore

In this study the linear driving force (LDF) model is chosen to estimate the micropore mass transfer coefficient, because the LDF model provides a reasonable prediction of the breakthrough curves for weakly adsorbed molecules in the composite zeolite pellet. Uptake in micropore is expressed as

$$\left(1-\varepsilon_p\right)\rho_s \frac{\partial w_k}{\partial t} = \left(1-\varepsilon_p\right)\rho_s K_{mic}(w_{msk}^* - w_k) \qquad (6)$$

The term on the right side of the equation describes the accumulation in micropore while the term on the left side of the equation describes the rate of mass transfer from macropore to micropore. The mass transfer coefficient, K_{mic}, is expressed as $K_{mic} = 15\frac{D_c}{r_c^2}$, where D_c and r_c are micropore diffusivity and radius of crystalline, relatively.

4.4.3 Uptake in Macropore

Uptake in macropore is expressed as

$$(1 - \varepsilon_i)\varepsilon_p \frac{\partial C_{msk}}{\partial t} + \left(1 - \varepsilon_p\right)\rho_s \frac{\partial w_k}{\partial t} = (1 - \varepsilon_p)\rho_s K_{mac}(w_{bk}^* - w_{msk}^*) \qquad (7)$$

The first term and the second term on the left side of the equation describe the accumulation in macropore and the mass transfer rate to the molecular sieve micropore respectively. And the term on the right side of the equation describes the rate of mass transfer from bulk gas. The mass transfer coefficient, K_{mac}, is expressed as $K_{mac} = 15\frac{D_{eff}}{r_p^2}$, where D_{eff} and r_p are effective diffusivity and adsorbent particle radius, relatively.

4.4.4 External fluid film resistance

The adsorbent particle is surrounded by thin external fluid film contributing to the overall mass transfer resistance at the outer surface of the pellet. The uptake rate is expressed by $\frac{\partial q}{\partial t} = \frac{3k_f}{R_P}(c_o - c^*)$ adapted from (Ruthven, 1994). It has been reported that "the external film resistance can be significantly reduced by increasing the flow rate of the fluid." [41]. In

this study, the external film resistance was minimized by employing a high superficial velocity.

4.4.5 Diffusion transport mechanisms

The rate of physical adsorption is commonly limited by diffusion transport rather than by the rate of equilibrium at a surface. The three different and most important types of diffusion mechanisms in physical adsorption [42] are:

- Bulk diffusion that is the predominant transport mechanism for large pores sizes when the mean free path of diffusing molecule is smaller than the pore opening of the adsorbent; molecule-wall collision is insignificant.

- Knudsen diffusion that is the predominant mechanisms when the mean free path of the diffusing molecule is much larger than the pore opening of the adsorbent; molecule-wall collision is significant.

- Surface diffusion, known as the micropore diffusion when the pore opening of the adsorbent is comparable with the size of the molecule.

4.4.6 Darcy's law

Darcy's law was used to predict the pressure gradient at a particular point in a bed. Darcy's law states that pressure drop is proportional to the gas superficial velocity. The relationship is expressed the equation (8):

$$\frac{\partial P}{\partial z} = -K_p v \tag{8}$$

where K_p is Darcy coefficient (in bar $\cdot$ s/m^2) and v is superficial gas velocity (in m/s).

4.5 Results and Discussion

Figure 4-5 shows the experimental breakthrough profiles of H_2 on the ½ inch OD column for the flow rate of 4030 sccm. The breakthrough time was plotted as a function of standard flow rates. The dead time was measured to be 17.9 seconds, which was the time that a gas molecule takes to pass through the breakthrough experimental setup with no adsorption. The long dead time might be mainly due to the mass flow meter, the long tubing and the valves consisting of the significant dead volume. The dead volume was calculated to be 718.3 cm^3. The dead volume is significantly large compared to both the volume of ½ OD bed and the volume of the 1 inch OD bed.
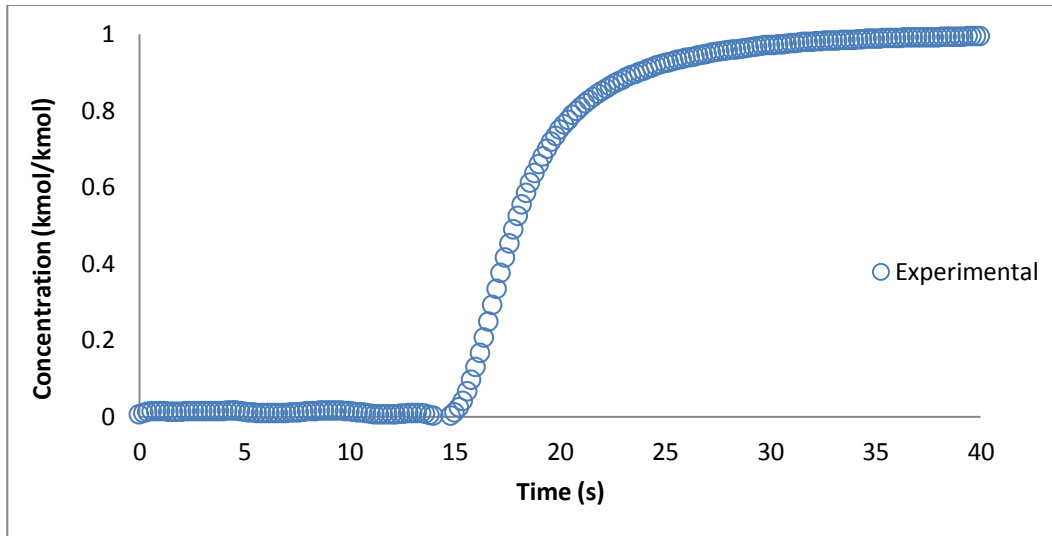
Figure 4-5. Experimental breakthrough profiles of H_2 on the $1/2$ inch OD column for the flow rate of 4030 standard cm^3/min

The dead volume is significantly larger than the volume of the packed bed, implying that the band broadening of the concentration profiles would be affected significantly by the dispersion caused by the dead volume, and the band broadening due to the dead volume has to be properly incorporated into the simulation. Therefore, the dead volume simulation was performed to take the diffusion effect of the dead volume and the dead time into account.

Figure 4-6 shows Comparison of experimental and simulated breakthrough profiles of H_2 on the $1/2$ inch OD column for the flow rate of 4030 sccm. The calculated dead volume was incorporated into simulation by employing different numbers of equal volume of tank voids in series. The process flow diagram for the dead volume simulation can be found in the Appendix 1.The assumption was made that the lumped sum of the dead

volumes of the flow meter, tubing, detector and valves can be predicted by the number of equal volume of tank voids in series. Solid lines represent higher number of tank voids in series while gradient lines represent the lower number of tank voids. The slope of the profile increases with increasing number of tank voids in series. It suggests that higher number of tank voids in series is required to take the effect of dead volume into account in the simulation. However, the 15 tank voids in series were selected to be employed in the simulation because increasing the number of tank voids took long simulation time and there is a negligible difference between the profiles using 15 tank voids and the one using 20 tanks. Thus, the 15 tank voids in series were incorporated into the simulation of CH_4 profile to measure the mass transfer coefficient of Na-ETS-10.
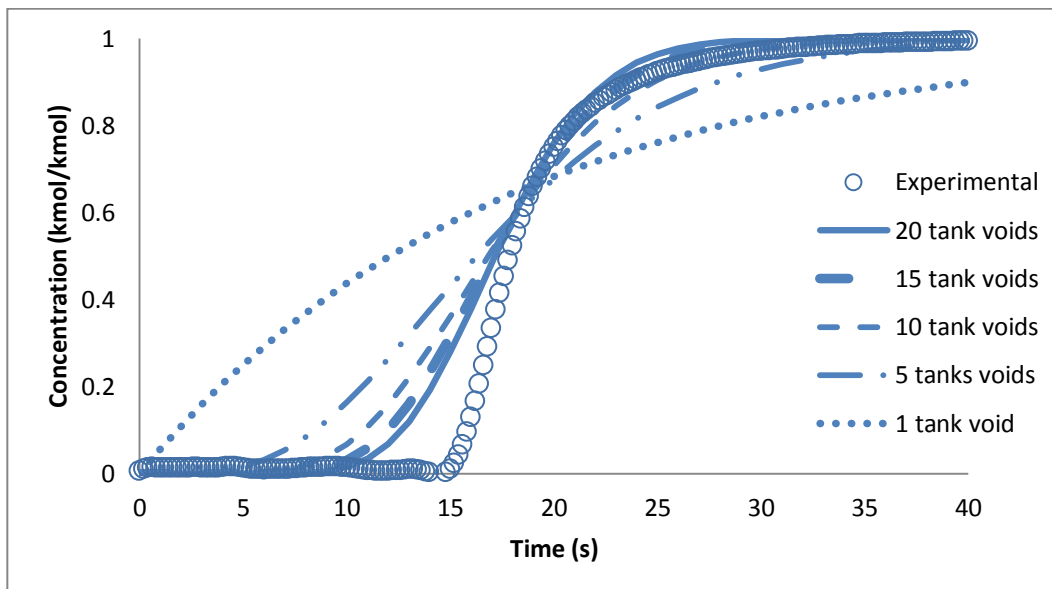
Figure 4-6. Comparison of experimental and simulated breakthrough profiles of H_2 on the $^1/_2$ inch OD column for the flow rate of 4030 sccm

Table 4-3 shows Experimental conditions of CH_4 breakthrough profiles on $^1/_2$ inch OD column for seven different flow rates.

Inlet Pressure (bar)	Temperature (K)	Volumetric flow [10^4] (sccm)
4.53	298.15	1.46
4.16	298.82	1.30
3.90	298.63	1.14
3.48	298.37	0.975
3.11	298.48	0.796
2.73	298.69	0.601
2.41	298.23	0.455

Table 4-3. Experimental conditions of breakthrough profiles on $^1/_2$ inch OD column for seven different flow rates

Figure 4-7 shows the comparison between experimental and predicted pressure drop across the ½ inch column for seven different flow rates at 25 °C. The pressure drops across the packed bed were significantly high because the particles were granule and, more importantly, the diameter of the bed was considerably small.
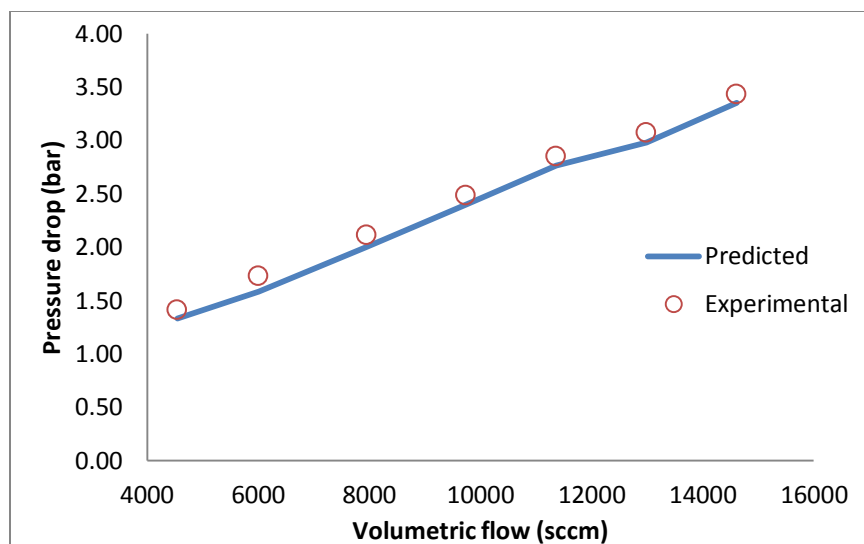
Figure 4-7. Comparison between experimental and predicted pressure drop across the $^1/_2$ inch OD column for seven different flow rates at 25 ^{o}C

Figure 4-8 shows the comparison between experimental, dead, adsorption and predicted breakthrough times on $^1/_2$ inch OD column for seven different flow rates. The breakthrough times were plotted as a function of standard flow rates. The adsorption times and the dead times slightly decrease with increasing flow rates. However, the adsorption times are significantly smaller than the dead time, implying that the dead volume is much larger than the adsorption capacities. It suggests that the band broadening of the concentration profiles due to the dead volume and the adsorption capacities have to be properly incorporated into the simulation. Furthermore, the predicted breakthrough times decrease considerably with increasing flow rates, because not only the adsorption time decreases with

increasing flow rates but also the dead time decreases with increasing flow rates. The predicted breakthrough times are reasonably in a good agreement with the experimental breakthrough times.
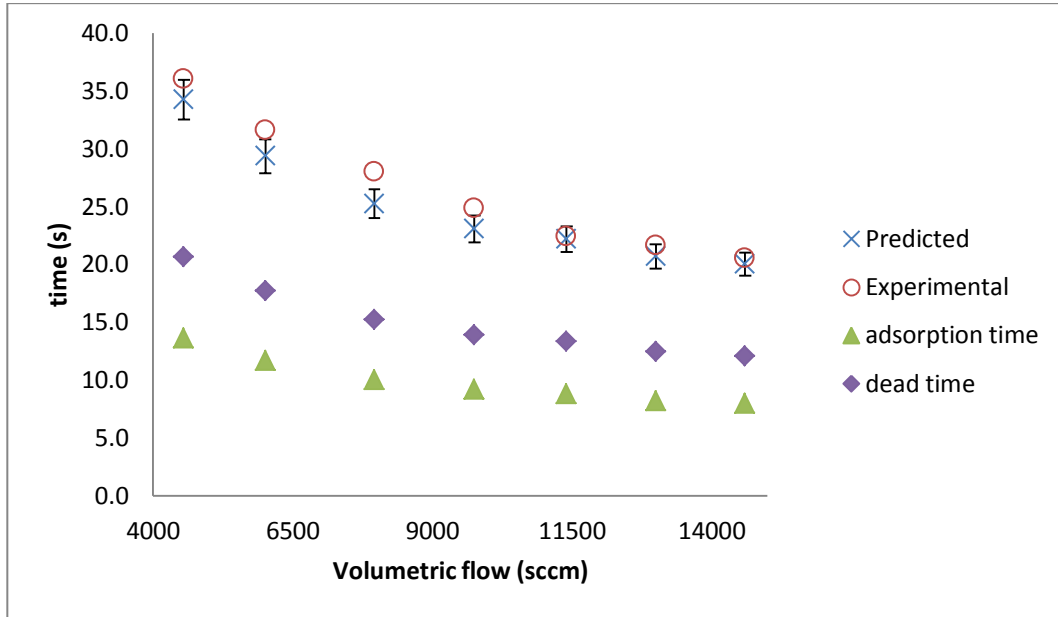
Figure 4-8. Comparison between adsorption time, dead time, experimental and predicted breakthrough times on the $^1/_2$ inch OD column for seven different flow rates

Figure 4-9 shows the comparison of dead volume, adsorption column, experimental and predicted breakthrough profiles of CH_4 on the $^1/_2$ inch OD column for the flow rate of 14600 sccm. The process flow diagrams for the Aspen adsorption simulation can be found in Appendix 1. The mean residence time for the dead volume profile is considerably smaller than one for the adsorption column profile. However, the band

broadening due to the dead volume is similar the band broadening due to the adsorption column, and their responses are much sharper than the experimental and predicted profiles. It suggests that the combined effects of the dispersion due to the dead volume and the band broadening due to the adsorption column are required to correctly estimate the mass transfer coefficient from the experimental profile. The experimental profiles were fitted using the Aspen Adsorption simulator by minimizing the global sum of square of errors between each experimental point and the model predicted point. The only adjustable tuning parameters were the macro/ micropore mass transfer coefficients, K_{mac} and K_{mic}. The K_{mac} and K_{mic} were estimated to be 245.643 (1/s) and 6129.332 (1/s), respectively. It captures the sharp front of the experimental profile at t < 19s, however, the experimental breakthrough profile exhibits a sharp front followed by a slight curvature at t > 22.8s, although the fitted breakthrough profile maintains the sharp front. The simulator was able to fit the sharp front but not able to capture the curvature following the sharp front even after incorporating 15 tank voids in series.
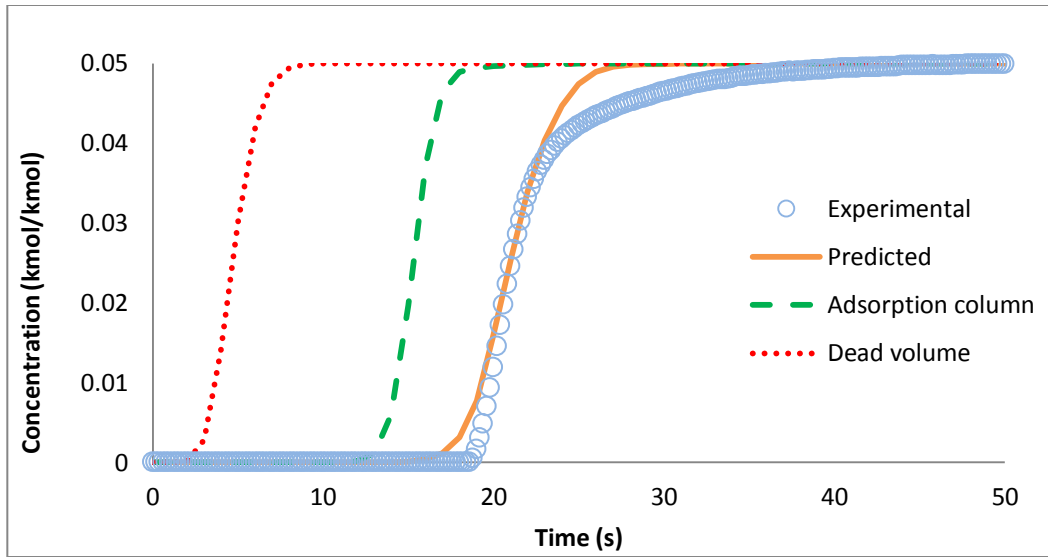
Figure 4-9. Comparison of dead volume, adsorption column, experimental and predicted breakthrough profiles of CH_4 on the $^1/_2$ inch OD column for the flow rate of 14600 sccm

Table 4-4 shows the estimated mass transfer coefficient of methane in pelletized Na-ETS-10 (the $^1/_2$ inch OD column for the flow rate of 14600 sccm).

Variable	magnitude	Units	Description
D_{eff}	$2.04·(10^{-6})$	m^2/s	Effective diffusivity of methane
D_c	$6.54·(10^{-9})$	m^2/s	Micropore diffusivity of methane
K_{mac}	245.643	1/s	Macropore mass transfer coefficient
K_{mic}	6129.332	1/s	Micropore mass transfer coefficient
τ	8.64		Tortuosity

Table 4-4. Mass transfer coefficient of methane in pelletized Na-ETS-10 (the $^1/_2$ inch OD column for the flow rate of 14600 sccm)

The estimated K_{mac} and K_{mic} were employed to predict the breakthrough profiles at the lower flow rates; Figure 4-10 shows the comparison of experimental and predicted breakthrough profiles of CH_4 on the ½ inch column at flow rates: 13000 sccm, 11400 sccm. 9750 sccm, 7960 sccm, 6010 sccm and 4550 sccm. The predicted responses estimate the experimental mean residence times well. However, each experimental breakthrough profile exhibits a sharp front followed by a slight curvature, although the predicted breakthrough profiles maintain the sharp front. The predicted profiles are fairly symmetric about their mean residence times while the experimental profiles are not. This might suggests that the simulator has the limitation in capturing the curvature with sharp front or the profiles with high nonlinearity parameter. Furthermore, the adsorption column profile is much sharper than the dead volume profile for the lower flow rates. This indicates that the dispersion effect due to the dead volume significantly affects the mass transfer coefficients more than the band broadening by the adsorption column does. It suggests that minimizing the dead volume will enable to estimate the mass transfer coefficient in the adsorbents more correctly. Overall, the reasonably acceptable predictions were generated by employing the same K_{mac} and K_{mic} values across a range of flow rates after taking the both effects of dead volume and the adsorption column into account.

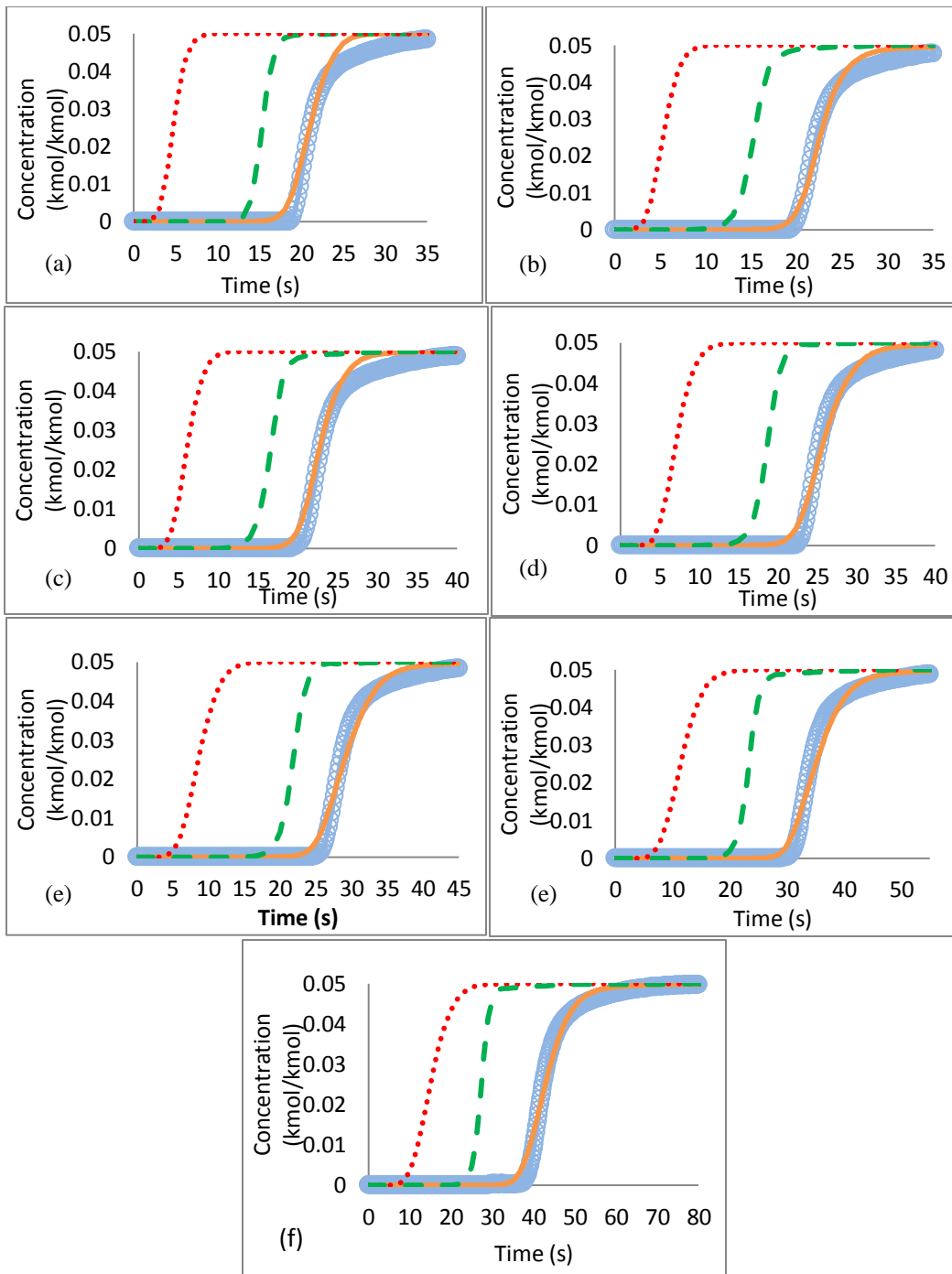Figure 4-10. Comparison of experimental and predicted breakthrough profiles of CH$_4$ on the $1/2$ inch OD column for the flow rate of (a) 14600 sccm (b) 13000 sccm (c) 11400 sccm (d) 9750 sccm (e) 7960 sccm (f) 6010 sccm (g) 4550 sccm

Table 4-5 shows Experimental conditions of CH_4 breakthrough profiles on 1 inch OD column for six different flow rates.

Inlet Pressure (bar)	T (K)	Volumetric flow [10^4] (sccm)
1.60	298.15	2.98
1.40	298.15	2.40
1.30	298.15	1.81
1.00	298.15	1.21
0.93	298.15	0.93
0.90	298.15	0.64

Table 4-5. Experimental conditions of breakthrough profiles on 1 inch OD column for six different flow rates

Figure 4-11 shows the comparison between experimental and predicted pressure drop across the 1 inch column for six different flow rates at 25 ^{o}C. The pressure drops across the packed bed were reasonably low because the diameter of the bed was long enough.
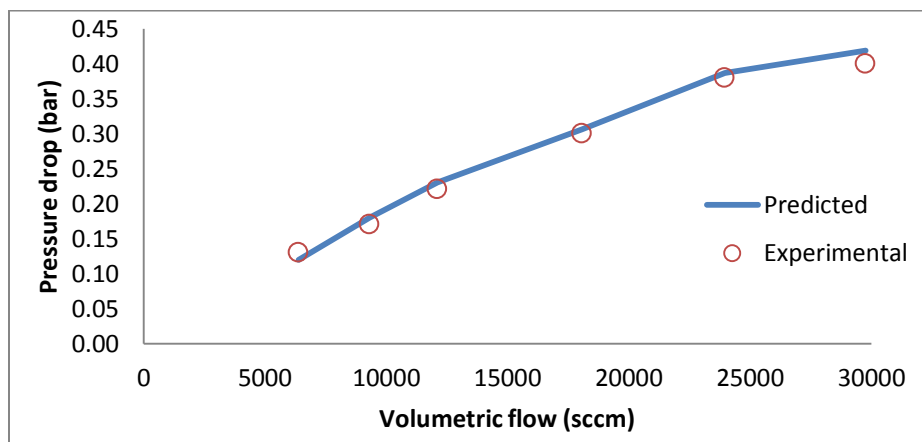

Figure 4-11. Comparison between experimental and predicted pressure drop across the 1 inch OD column for six different flow rates at 25 ^{o}C

Figure 4-12 shows the comparison between experimental and predicted breakthrough times on 1 inch OD column for the six different flow rates. The breakthrough time were plotted as a function of standard flow rates. The adsorption times and the dead times decrease with increasing flow rates. Furthermore, the adsorption times are significantly bigger than the dead time, implying that the dead volume is much smaller than the adsorption capacities. This indicates that the band broadening due to the adsorption column significantly affects the predicted and experimental breakthrough profiles more than the dispersion effect of the dead volume does. It suggests that 1 inch OD column is more suitable for the correct estimation of the mass transfer coefficient in the adsorbents. Furthermore, the predicted breakthrough times decrease considerably with increasing flow rates, because not only the adsorption time decreases with increasing flow rates but also the dead time decreases with increasing flow rates. The predicted breakthrough time also display error bars with 5%. The experimental capacities are in within 5% errors of the predicted capacities, which validate the experimental data. Thus, the predicted breakthrough times are reasonably in a good agreement with the experimental breakthrough times.
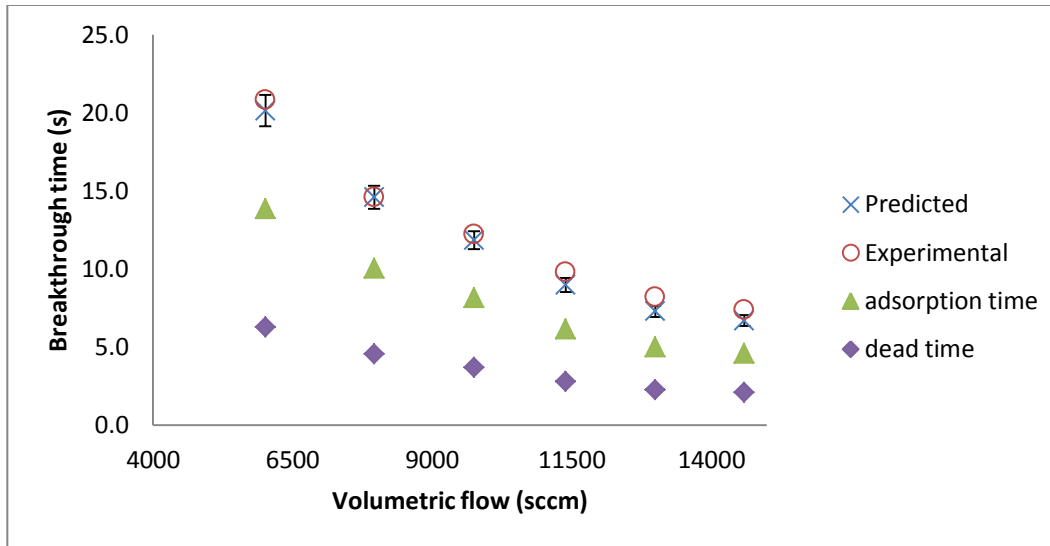
Figure 4-12. Comparison between experimental and predicted breakthrough times on the 1 inch OD column for six different flow rates at 25 $^{\circ}$C

Figure 4-13 shows the comparisons of dead volume, adsorption colum, experimental and simulated breakthrough profiles on 1 inch OD colum for the flow rate of 29800 sccm. The mean residence time for the dead volume profile is considerably smaller than one for the adsorption column profile. Additionally, the band broadening due to the dead volume is much sharper than the band broadening due to the adsorption column; however, the band broadening due to the adsorption column is similar to the slopes of the experimental and predicted profiles. It suggests the estimation of the mass transfer coefficients from the experimental profile would more correctly reflect the kinetics of methane in the adsorbents. The experimental profile for a flow rate of 29800 sccm was fitted using the Aspen simulator by minimizing the global sum of square of errors between each

experimental point and the model predicted point. The only adjustable tuning parameters were the macro/ micropore mass transfer coefficients, K_{mac} and K_{mic}. The K_{mac} and K_{mic} were estimated to be 261.761 (1/s) and 6121.874 (1/s), respectively. It captures the sharp front of the experimental profile at t < 8.6s, however, the experimental breakthrough profile exhibits a sharp front followed by a slight curvature at t > 9.0s, although the fitted breakthrough profile maintains the sharp front. The simulator was able to fit the sharp front but not able to capture the curvature following the sharp front even after incorporating 15 tank voids in series.
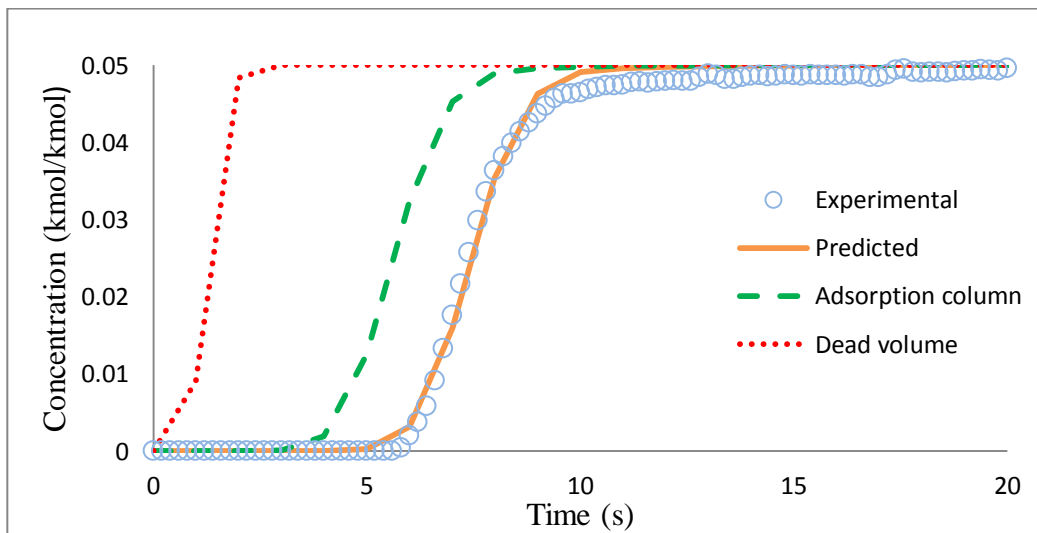

Figure 4-13. Comparison of experimental and simulated breakthrough profiles of CH_4 on the 1 inch OD column for the flow rate of 29800 sccm

Table 4-6 shows the estimated mass transfer coefficient of methane in pelletized Na-ETS-10 (the 1 inch OD column for the flow rate of 29800 sccm).

Variable	magnitude	Units	Description
D_{eff}	$7.66 \cdot (10^{-6})$	m^2/s	Effective diffusivity of methane
D_c	$6.53 \cdot (10^{-9})$	m^2/s	Micropore diffusivity of methane
K_{mac}	261.76	$1/s$	Macropore mass transfer coefficient
K_{mic}	6121.87	$1/s$	Micropore mass transfer coefficient
τ	2.76		Tortuosity

Table 4-6. Mass transfer coefficient of methane in pelletized Na-ETS-10 (the 1 inch OD column for the flow rate of 29800 sccm)

The micropore diffusivity of methane in Na-ETS-10 was estimated to be $6.53 \cdot 10^{-9}$ m^2/s, which was considerably smaller than the effective diffusivity of methane. However, the path length in the crystal was significantly smaller than the path lengths in composite the particle. The macropore and micropore mass transfer coefficients are 261.76 (1/s) and 6121.87 (1/s), respectively, which suggests that the macropore mass transfer coefficient is dominant in the pelletized form of Na-ETS-10. Thus, the macropore mass transfer coefficient is limiting the adsorption dynamics of ETS-10 loaded column.

Mitchell and Gallo predicted the self-diffusion coefficient of methane in ETS-10 as a function of loading using equilibrium molecular dynamics simulations. Their predicted self-diffusion coefficient of methane ranged from $57 \cdot (10^{-9})$ m^2/s to $7.3 \cdot (10^{-9})$ m^2/s (Mitchell and Gallo, 2004). Our estimated micropore diffusivity of methane in pelletized Na-ETS-10 is $6.53 \cdot (10^{-9})$ m^2/s, which is reasonable in agreement with the literature values.

The estimated K_{mac} and K_{mic} were employed to predict the breakthrough profiles at the lower flow rates; Figure 4-14 shows the comparison of experimental and predicted breakthrough profiles of CH_4 on the ½ inch column at flow rates: 29800 sccm, 24000 sccm, 18100 sccm, 12100 sccm, 9320 sccm and 6380 sccm. The predicted responses estimate the experimental mean residence times well. However, each experimental breakthrough profile exhibits a sharp front followed by a slight curvature, although the predicted breakthrough profiles maintain the sharp front. The predicted profiles are fairly symmetric about their mean residence times while the experimental profiles are not. This also proves that the simulator has the limitation in capturing the curvature with sharp front or the profiles with high nonlinearity parameter. Furthermore, the dead volume profile is much sharper than the adsorption profile for the lower flow rates. This indicates that the dispersion effect due to the dead volume is not as significant as the band broadening of the adsorption column profiles for estimating the mass transfer coefficient. Thus, the band broadening due the adsorption column closely reflects the effects of the mass transfer coefficients. It also suggests that having bigger adsorption capacities than the dead volume would enable to estimate the mass transfer coefficient in the adsorbents more correctly. Overall, the reasonably good predictions were generated by employing the same K_{mac} and K_{mic} values across a range of flow rates.
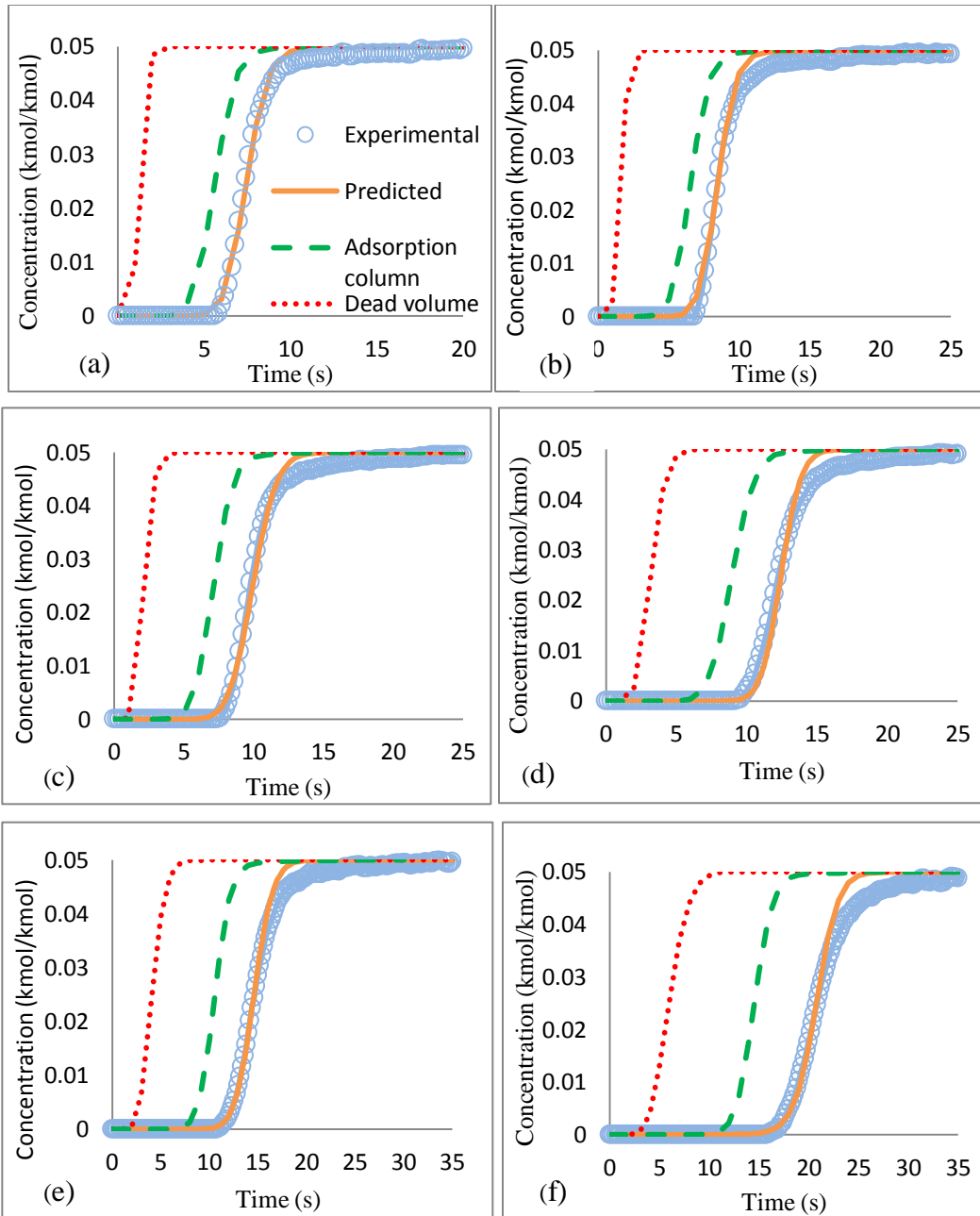
Figure 4-14. Comparison of experimental and simulated breakthrough profiles of CH_4 on the 1 inch OD column for the flow rate of (a) 29800 sccm (b) 24000 sccm (c) 18100 sccm (d) 12100 sccm (e) 9320 sccm (f) 6380 sccm

4.6 Conclusion

This study has demonstrated that the macropore resistance is limiting the adsorption dynamics in the Na-ETS-10 pellet. A breakthrough concentration profile of diluted (5+%) methane balance helium was obtained at 100 kPa and 25 ℃ and was fitted with Aspen adsorption simulator using the macro/ micropore mass transfer coefficients as the adjustable tuning parameters. The macropore and micropore mass transfer coefficients are 261.76 (1/s) and 6121.87 (1/s), respectively. These results are very encouraging as they suggest the existing particles are sufficiently "fast" to be used in an adsorption process near the fluidization limit of the particles. The current data also suggests that improvements in bed density are likely possible by increasing the density of the composite particle.

The future work will be also necessary to carry out more the breakthrough experiments on a bigger range of pellet sizes of Na-ETS-10 in order to confirm the macropore rate. Furthermore, the performance of densified ETS-10 aggregates will be needed to be investigated for the macropore / micropore diffusion rate.

References

[1] Levan, M. D., 1998, Adsorption processes and modeling: present and future, in Fundamentals of Adsorption. Elsevier

[2] Kulprathipanja, S., 2010, Zeolites in industrial separation and catalysis. John Wiley & Sons

[3] Avila, A. M., Yang, F., Shi, M., Kuznicki, S. M., 2011, Extraction of ethane from natural gas at high pressure by adsorption on Na-ETS-10, Chemical Engineering Sicence, 66, 2991-2996

[4] Anson, A., Lin, C. H., Kuznicki, T. M., Kuznicki, S. M., 2009, Separation of ethylene/ ethane mixtures by adsorption on small-pored titanosilicate molecular sieves, Chemical Engineering Science, 65, 807-811

[5] Jee, J. G., Kim, M. B., Lee, C. H., 2005, Pressure swing adsorption processes to purify oxygen using a carbon molecular sieve, Chemical Engineering Science, 60, 869-882

[6] Rousseau, R. W., 1987, Handbook of separation process technology. John Wiley & Sons

[7] McCuster, L. B., Baerlocher, C., 2007, Zeolite structures, in Introduction to zeolite science and practice. Elsevier

[8] Galioglu, S., Zahmakiran, M., Eren, K. Y., Ozkar, S., Akata, B., 2012, Effect of silver encapsulation on the local structure of titanosilicate ETS-10. Microporous and Mesoporous Materials, 159, 1-8

[9] Kuznicki, S. M., 1991. Large-pored crystalline titanium molecular sieve zeolites. US Patent No. 5,011,591

[10] Anson et al., 2008, Adsorption of ethane and ethylene on modified ETS-10, Chemical Engineering Sciences, 63, 4171-4175

[11] Anson et al, 2008, Adsorption of argon, oxygen, and nitrogen on silver exchanged ETS-10 molecular sive, Microporous and Mesoporous Materials, 109, 577-580

[12] Macedonia, M. D., Moore, D. D., Maginn, E. J., Olken, M. M., 1999, Adsorption studies of methane, ethane, and argon in the zeolite mordenite: Molecular simulations and experiments, Langmuir, 16, 3823-3834

[13] Dunne, J. A., Myers, A. L., Kofke, D. A., 1996, Simulation of adsorption of liquid mixtures of N_2 and O_2 in a model faujacite cavity at 77.5 K, Adsorption, 2, 41

[14] Tassel, V. T., Davis, H. T., McCormick, A. V., 1994, Adsorption simulations of small molecules and their mixtures in a zeolite micropore, Langmuirs, 10, 1257-1267

[15] Thomson, K. T., McCormick, A. V., Davis, H. T., 2000, The effects of a dynamic lattice on methane self-diffusivity calculations in $AlPO_4$-5, Journal of Chemical Physics, 112, 3345-3350

[16] Todd, R. S., Webley, P. A., 2005, Macropore diffusion dusty-gas coefficient for pelletised zeolites from breakthrough experiments in the O_2/N_2 system, Chemical Engineering Science, 60, 4593-4608

[17] Ruthven, D. M., Farooq, S., Knabel, K. S., 1994, Pressure swing adsorption, wiley-VCH

[18] Kern, W., 1993, Handbook of semiconductor wafer cleaning technology- science, technology, and applications, William Andrew

[19] Balbuena, P. B., Gubbins, K. E., 1993, Theoretical interpretation of adsorption behavior of simple fluids in slit pores, Langmuir, 9, 1801-1814

[20] Yang, R. T., 1987, Gas separation by adsorption processes, Butterworth

[21] Cejka, J., Bekkum, H. V., Corma, A., Schuth, F., 2007, Introduction to zeolite science and practice, Elsevier

[22] Shi, Meng., Kim, J., Sawada, J., Lam, J., Sarabadan, S., Kuznicki, T., Kuznicki, S., 2012, Production of argon free oxygen by adsorptive air separation on Ag-ETS-10. American Institute of Chemical Engineers, DOI: 10.1002/aic.13879

[23] Smith, A.R., Klosek, J., 2001. Fuel Processing Technology 70, 115-134

[24] Talu, O., Li, J., Kumar, R., Mathisa, P.M., Jr, J.D.M., Schork, J.M., 1996, Gas separation & purification, 10, 149-159

[25] Moon, I.S., Lee, D.I., Yang, J.H., Ryu, H.W., 1986, Korean Journal of Chemical Engineering, 3, 15-21

[26] Jee, J.G., Lee, S.J., 2005, Adsorption, 11, 415-420

[27] Zahara, M., Jafa, T., Masoud, M., 2008, World Academy of Science, Engineering and Technology, 47, 99-103

[28] Reid, C.R., O'koye, I.P., Thomas, K.M., 1998, Langmuir, 14, 2415-2425

[29] Tan, J.S., Ani, F.N., 2004, Separation & Purification Technology, 35, 47-54

[30] Jee, J. G., Lee, S.J., Lee, C.H., 2004. Korean Journal of chemical engineering, 21, 1183-1192

[31] Rutherford, S.W., Coos, J.E., 2005, Journal of Colloid and Interface Science, 284, 432-439

[32] Jee, J.G., Kim, M.B., Lee, C.H., 2005, Chemical Engineering Science, 60, 869-882

[33] Anson, A., Kuznicki, S.M., Kuznicki, T.M., Dunn, B.C., Eyring, E.M., Hunter, D.B., 2009, Separation Science & technology, 44, 1604-1620

[34] Hayashi, S., Kawai, M. Kaneko, T., 1996, Gas separation & Purification

[35] Boniface, H.A., 1983, Ph.D thesis, the University of New Brunswick, Fredericton, Canada

[36] Sebastian, J., Jasra, R.V., 2005, Industrial & Engineering Chemistry Research, 44, 8014-8024

[37] Habgood, H.W., 1964, Canadian Journal of Chemistry, 42, 2340-2350

[38] Huston, N.D., Rege, S.U., Yang, R.T., 1999, AICHE Journal, 45, 724-734

[39] Dee, D.P., Chiang, R.L., Miller, E.J., Whitley, R.D., 2003, High purity oxygen production by pressure swing adsorption, US patent No. 6,544318 B2

[40] Anson, A., Kuznicki, S.M., Kuznicki, T.M., Haastrup, T., Wang, Y., Lin, C.C.H., Sawada, J.A., Eyring, E.M., Hunter, D., 2008, Microporous mesoporous materials, 109, 577-580

[41] Rao, D. G., 2010, Introduction to Biochemical Engineering second edition, Tata McGraw Hill Education Private Limited

[42] Mota, J. P., 2004, Adsorption and Transport in nanoporous materials. In Lu, G. Q., Zhao, X. S., (Eds.), Nanoporous Maetirals – Science and Engineering, 694-726, World Scientific
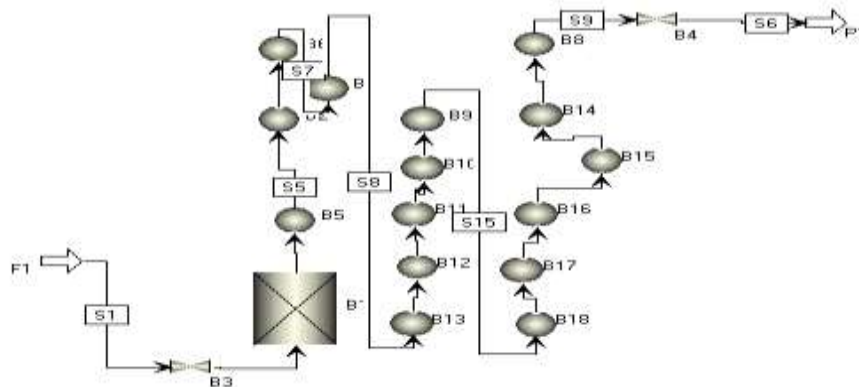
Appendix 1

1. Process flow sheet for the dead volume simulation
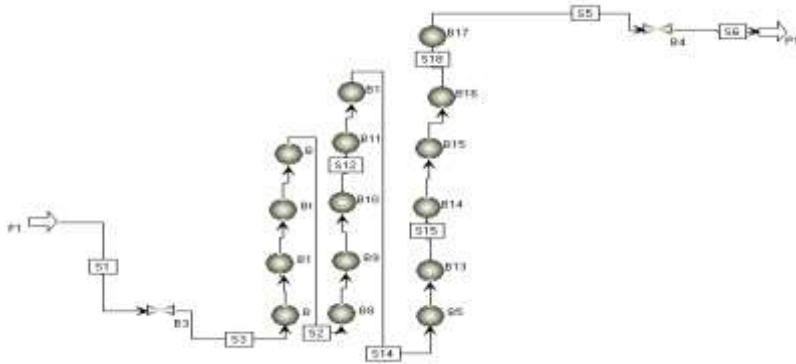
2. Process flow sheet for the adsorption column only
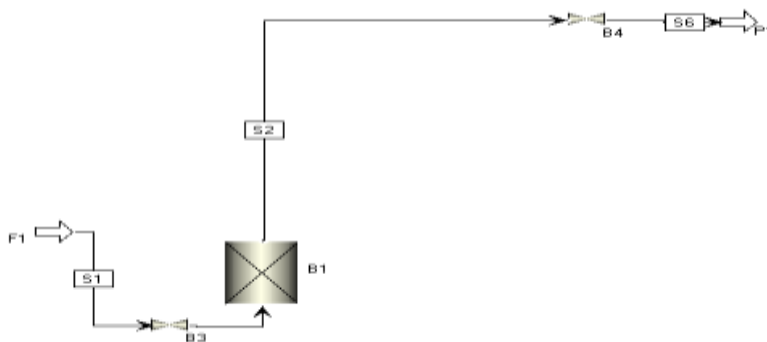
3. Process flow sheet for the adsorption column with the dead volume incorporated

Appendix 2

Copyrighted materials permissions:

Order Details

Licensee: Jihong Kim

License Date: Feb 28, 2013

License Number: 3097610089681

Publication: Elsevier Books

Title: Studies in Surface Science and Catalysis, Volume 168

Type Of Use: reuse in a thesis/dissertation

Total: 0.00 USD

Order Details

Licensee: Jihong Kim

License Date: Feb 28, 2013

License Number: 3097620546429

Publication: Chemical Engineering Science

Title: Extraction of ethane from natural gas at high pressure by adsorption

on Na-ETS-10

Type Of Use: reuse in a thesis/dissertation

Total: 0.00 USD

Order Details

Licensee: Jihong Kim

License Date: Feb 28, 2013

License Number: 3097650041715

Publication: Microporous and Mesoporous Materials

Title: Adsorption of argon, oxygen, and nitrogen on silver exchanged ETS-10 molecular sieve

Type Of Use: reuse in a thesis/dissertation

Total: 0.00 USD

Order Details

Licensee: Jihong Kim

License Date: Feb 28, 2013

License Number: 3097650458949

Publication: AIChE Journal

Title: Production of argon free oxygen by adsorptive air separation on Ag-ETS-10

Type Of Use: Dissertation/Thesis

Total: 0.00 USD